

THE RF-CONTROLLED CATHODE: MODELING
AND LARGE-DIAMETER CATHODE
EXPERIMENTAL RESULTS

MATTHEW L. PLASEK

A DISSERTATION
PRESENTED TO THE FACULTY
OF PRINCETON UNIVERSITY
IN CANDIDACY FOR THE DEGREE
OF MASTERS OF SCIENCE IN ENGINEERING

RECOMMENDED FOR ACCEPTANCE
BY THE DEPARTMENT OF
MECHANICAL AND AEROSPACE ENGINEERING
ADVISER: PROFESSOR EDGAR Y. CHOEIRI

JANUARY 2016

© Copyright by Matthew L. Plasek, 2016.

All rights reserved.

Abstract

A promising thermionic hollow cathode concept is investigated through both numerical modeling and experiment for application to high-power, long-lifetime electric thrusters. This new RF-Controlled Cathode concept adds radio-frequency power to a large-diameter cathode to benefit the internal plasma structure. Finite-element analysis was performed on a simplified two-dimensional model to find that with increasing RF power, the axial plasma density profile increased and its peak shifted upstream, resulting in improved emitter utilization and maximum discharge current. A mode transition which sharply pronounces these effects was found to occur due to a resonant cavity condition and a resulting increase to the reduced electric field E/n_0 (the ratio of field to gas densities). Experimentally, a large-diameter cathode was tested at discharge currents of 20 to 225 A on the developmental path to RF power addition. Current-voltage characteristics and axial temperature profiles were measured across discharge currents, mass flow rates, and gas species. Measured current-voltage characteristics follow expected trends, though orifice-plate temperatures measured during operation are found to be approximately 1000 °C lower than the next-largest cathodes in the literature. Finally, both thermal and cathode heater design are identified as key challenges for large-diameter cathodes and relevant experimental findings are discussed.

Acknowledgements

I first must acknowledge my dear fiancée Allie. Please know that twenty versions of this paragraph would do no better than two hundred in thanking you for everything in the past four years and for everything to come in the next (few) hundred. I look forward to continuing our adventures around the Earth and eventually to another celestial body or two.

This thesis would not have been possible without my advisor, Professor Edgar Choueiri. I thank you for proving to me that a “Renaissance Man” approach to life is the only way to go. Whether noting that aesthetics and the functional can indeed coexist or that ten versions of an abstract is not too many, I will always be grateful for your standard-setting as it has only helped me raise my own.

There would be no experiment without Bob Sorenson’s masterful maker instincts and skill. Under your watch I learned more about how things are made, how things are supposed to work, and how I could actually make them work than I ever expected possible in my few short years in the lab. If I know anything about manufacturing (or many other topics) it is because you got me started.

For being an expert resource I would like to thank collaborator Dr. James E. Polk from JPL. Jay’s valuable feedback and experience significantly aided in the construction of a new cathode experiment. For expanding my plasma horizons and bridging plasma labs, I would like to thank Professor Sam Cohen and Dr. Yvegeny Raitses. In addition, my thanks to the Keller Center team as well as the MAE faculty who supported me.

I am happy to give a shout out to my fellow labmates I was lucky enough to get to know and who share my passion of the final frontier: Justin, Matt, and Ben for not only collaborating in countless struggles but making the lab much more than a chilled, fluorescent home away from home. I look forward to seeing all of your famous advances in the future, in EP or otherwise. Thank you Chris and Sebastián

for enduring my sleep-deprived self and for helping to create a working (!) cathode, especially in the hectic final months. Chris, I hope you get to answer the questions I started with and thanks to summer student Nicolas for getting an eyeful of the pyrometer. Pat, Will, and Mike, you engendered determination, exuded enthusiasm, and brought new humor into the lab which I greatly appreciated, and visiting students Lorenzo and Jaume, I am still impressed by your execution while visiting.

To even get to the point of writing a thesis, I must acknowledge my brother Aaron for the many long conversations, middle-of-the-night help, and most importantly, for continually holding me to my dreams. I am also very thankful for the many sessions where I was flanked by my classmates who helped me muddle through the thick of it and come out (mostly) alive.

Finally, my dear thanks to my parents Larry and Ardell, who abolished “rest” from their dictionaries long ago and supported me to follow my passions whichever way they pointed.

This research was made possible with support from the U.S. Air Force Office of Scientific Research and benefited from collaboration with the NASA Jet Propulsion Laboratory. This dissertation carries T-3270 in the records of the Department of Mechanical and Aerospace Engineering.

Contents

Abstract	iii
Acknowledgements	iv
List of Figures	viii
List of Symbols	xiv
1 Introduction	1
1.1 Motivation and Background	1
1.1.1 Why do cathodes matter?	1
1.1.2 Why do we need better cathodes?	2
1.1.3 A glimpse inside hollow cathode fundamentals	5
1.2 A Brief Review of the Recent Literature	8
1.2.1 Methods to Increase Life and Discharge Current	8
1.2.2 Energetic Ion Mitigation and RFC Cathode Relevance	11
1.3 Thesis Objectives and Organization	14
2 Concept Exploration and Design	16
2.1 Conceptual Design	16
2.1.1 Selection of an Emitter Insert Composition	17
2.1.2 Two-Stage Configuration	18
2.1.3 Single-Stage Configuration	19
2.1.4 Comparison of Configurations	22

2.2	Selected Design Considerations	24
2.2.1	Adding RF Power to a Thermionic Hollow Cathode	25
2.2.2	Cathode Size	27
3	Numerical Modeling	30
3.1	Schematic and Computational Grid	30
3.2	Computational Model	31
3.3	Results and Discussion	37
3.3.1	Explanation of Nonlinear Transition Behavior	44
3.3.2	Hysteresis and Post-Transition Stability	49
3.4	Chapter Summary	51
4	Experiment	55
4.1	Design Features of the RFC Cathode	55
4.1.1	Novel Cathode Design	56
4.2	Experimental Setup	59
4.3	Diagnostics	63
4.4	Operational Ignition Procedure	65
4.5	Experimental Results and Discussion	66
4.5.1	Ignition and Non-RF Operation	66
4.5.2	Heater Failure Modes	72
5	Conclusions	75
5.1	Summary of Major Findings	76
5.1.1	Numerical Modeling Findings	76
5.1.2	Experimental Findings	77
5.2	Recommendations for Future Work	79
	Bibliography	82

List of Figures

1.1	Side cutaway views of a basic hollow cathode showing the typical limited current attachment area along the length of the LaB ₆ emitter (left) compared to the goal of current attachment to the full emitter area (right). The red arrow depicts the axial extent of the current attachment.	7
1.2	Side cutaway view of a typical thermionic hollow cathode setup. . . .	8
2.1	Two-stage configuration of the RFC Cathode LaB ₆ hollow cathode with the dielectric pre-stage on the left, encircled by a RF antenna. RF power is deposited near the upstream insert region, inside the pre-stage. The red arrow depicts the axial extent of the current attachment.	19
2.2	Single-stage configuration of the RFC-Cathode LaB ₆ hollow cathode with the upstream end mated to a circular waveguide. RF power is deposited in the plasma near the upstream insert end after traveling through the microwave window.	19
2.3	Single-stage configuration of the RFC-Cathode LaB ₆ hollow cathode with the upstream end on the left, mated with a coaxial cable. RF power arrives from the left where power is deposited in the plasma near the upstream insert end.	20

2.4	Maximum electron current density at the emitter wall as a function of plasma density. Argon gas and an electron temperature of 1 eV are assumed.	25
2.5	Electron plasma frequency corresponding to plasma density. A plasma density of about $8 \times 10^{17} \text{ m}^{-3}$ will reflect incident microwaves of 8 GHz.	27
3.1	RFC Cathode Schematic Representation	31
3.2	RFC Cathode Computational Grid, refined near regions of expected sharp transition, such as the plasma-surface boundaries and the microwave window.	32
3.3	Plasma density profiles versus distance from the microwave window for a uniform pressure of 1.5 Torr (corresponding to an argon flow rate of 40 SCCM). As the RF power increases, a significant plasma density extends further upstream (shown by the bold arrow). The upstream microwave window edge is on the left (Distance From Window = 0 cm), while the downstream orifice is on the right (Distance From Window = 9.0 cm).	38
3.4	Plasma density profiles versus distance from the microwave window for a uniform pressure of 1.5 Torr (corresponding to an argon flow rate of 40 SCCM). As the RF power increases further, plasma density increases preferentially at the axial depth of the maximum plasma density and peak emitter temperature. The upstream microwave window edge is on the left (Distance From Window = 0 cm), while the downstream orifice is on the right (Distance From Window = 9.0 cm).	40

3.5	Plasma density profiles versus distance from the microwave window for a uniform pressure of 2.5 Torr (corresponding to an argon flow rate of 110 SCCM). As the RF power increases, a significant density extends further upstream (shown by the bold arrow). The upstream microwave window edge is on the left (Distance From Window = 0 cm), while the downstream orifice is on the right (Distance From Window = 9.0 cm).	41
3.6	Plasma density profiles versus distance from the microwave window for a uniform pressure of 2.5 Torr (corresponding to an argon flow rate of 110 SCCM). As the RF power increases further, plasma density increases preferentially near the depth of the maximum plasma density. The upstream microwave window edge is on the left (Distance From Window = 0 cm), while the downstream orifice is on the right (Distance From Window = 9.0 cm).	42
3.7	A two-dimensional representation of the plasma density profile versus distance from the microwave window corresponding to the curves in Figure 3.5. The three plots are using the same color scaling to compare increasing RF powers moving down with (a) 0 W, (b) 10 W, and (c) 20 W. Note that the centerline plasma density is increasing and the densest region moves upstream with increasing RF power. Surface plots of the emitter temperature are shown in grayscale above and below the plasma density surface plots.	43
3.8	Continuing the increase in RF power from Figure 3.7, this two dimensional plot has an incident RF power of 30 W and has made a significant, sharp increase in plasma density. This figure has a different color scaling than the pre-transition plots in Figure 3.7. Surface plots of the emitter temperature are shown in grayscale above and below the plasma density plot.	44

3.9	Emitted current versus RF power for five different flow rates corresponding to pressures used in our simulations. Note the clear increase in emitted current and the critical transition point's dependence on RF power and flow rate.	45
3.10	Progression of the critical electron density ($8 \times 10^{17} \text{ m}^{-3}$) contour with increasing RF power, showing the transition occurring as the critical density reaches the upstream window.	47
3.11	RF electric field amplitude curves for different RF powers as a function of waveguide position. At a critical RF power the electric field amplitude sharply increases in magnitude due to a cavity resonance condition. Note that the structure of the electric field amplitude changes significantly after the transition.	48
3.12	The reflection coefficient as a function of input RF power and pressure. Note the larger dip at the transition for higher pressures, corresponding to more efficient power absorption. At low RF powers and low pressure (1.5 Torr), the plasma density is below the critical density for RF reflection.	49
3.13	The reduced electric field amplitude E/n_0 for different input RF powers, with these four cases matching those in Fig. 3.10. The reduced electric field increases with RF power as the skin depth decreases. . .	50
3.14	The average electron number density over the simulated emitter area is shown as a function of input RF power as the RF power is increased from 0 to 100 W and then slowly reduced to 0 W. The nonlinear transition behavior as the input power is increased and the hysteresis in the plasma density as the power is decreased are both evident. The low RF power range ($< 20 \text{ W}$) of the upper branch may not have reached a steady-state solution.	51

3.15	RF electric field amplitude curves for different waveguide lengths. At a critical waveguide length (4.0 cm in this case) for a fixed RF power (100 W), the electric field amplitude sharply increases in magnitude due to a cavity resonance condition. Note that the structure of the electric field amplitude repeats itself as the waveguide length continues to be increased.	52
4.1	Side cutaway views of the RFC Cathode created in CAD software. The purple region in the top image is the LaB ₆ emitter tube insert. In the bottom image, the orange arrows depict microwave propagation in waveguide, light blue arrows depict the neutral gas injection path, and the red overlay is the emitter region and internal cavity. Plasma exits downstream through the orifice to the right. The heater and heater radiation shielding are not pictured.	57
4.2	A side cutaway view of emitter region of the RFC Cathode.	60
4.3	The RF-Controlled Hollow Cathode experiment installed in the tank.	61
4.4	An electrical diagram for the RFC Cathode experiment.	62
4.5	The RFC Cathode operating at high discharge current on the left and at a lower current on the right. The downstream anode exit is at the left in the photos and the cathode is on the right. Although not distinguishable, the cathode plume is forming a few-centimeter diameter beam just beyond the keeper plate, signaling “jet” mode operation.	66
4.6	Locations of temperature measurements. 1-3 in red are pyrometer measurement locations (1 is the window, 2 is the heater wire, and 3 is the orifice plate) and 4-7 in blue are thermocouple measurements of the outer graphite surface of the cathode emitter region. (Slots exist in the boron nitride insulators for the thermocouples to touch the cathode wall directly.)	67

4.7	Temperature measurements taken prior to plasma ignition as a function of the distance from the inner surface of the orifice plate along the cathode major axis. 1-3 in red are pyrometer measurements (1 is the microwave window, 2 is the heater wire, and 3 is the orifice plate) and 4-7 in blue are thermocouple measurements of the outer cathode surface.	68
4.8	Discharge initiation voltage as a function of internal mass flow rate in SCCM for selected operating points using argon and krypton gas. . .	69
4.9	A comparison of the anode and keeper voltages versus mass flow rate for argon and krypton at approximately 20 A anode current.	69
4.10	A comparison of peak thermocouple measurements versus mass flow rates of krypton and argon. The mass flow rates for each gas are offset from each other due to different flow meter corrections for each gas. .	70
4.11	Anode and keeper voltages versus anode current for operation with krypton. The keeper current was held constant at 2.2 A and the mass flow rate was fixed at 42 SCCM. The measurement error bars are smaller than the plot markers used.	71
4.12	Thermocouple temperatures vs discharge current at a constant mass flow rate of 42 SCCM and 2.2 A keeper current.	72
4.13	Pictured are examples of damaged boron nitride rings (left) and broken tungsten heater wire (right).	74

List of Symbols

A_0	Theoretical Richardson-Dushman coefficient
D_0	Experimentally modified value of A_0
E	Electric field
J_{te}	Thermionic emission current density
J_i	Ion current density
J_e	Electron current density
J_r	Random electron current density
M_i	Ion (or neutral) mass
P_r	Microwave power reflected
P_i	Microwave power incident
T	Thermionic insert temperature
T_w	Thermionic insert temperature
T_e	Plasma electron temperature
X'_{11}	Cutoff frequency constant
a	Internal cathode radius or waveguide radius
c_0	Speed of light in vacuum
\bar{c}_e	Electron thermal velocity
e	Electron charge
f_{co}	Cutoff frequency in a waveguide
$f_{co,coax}$	Cutoff frequency for a coaxial waveguide

$f_{\text{co,wg}}$	Cutoff frequency for a cylindrical waveguide
f_{source}	Frequency of the RF source
k or k_{B}	Boltzmann's constant
m_{e}	Electron mass
\dot{m}	Mass flow rate
n_0	Neutral gas density
n_{c}	Cutoff plasma density
n_{e}	Electron number density
n_{i}	Ion number density
n_{sw}	Plasma density required for surface waves
\dot{q}'''	Joule heating of emitter material
q_{e}''	Heat flux due to electron current
q_{ex}''	Heat flux due to wall de-excitation
q_{i}''	Heat flux due to ion current
q_{te}''	Heat flux due to thermionic emission
q_{wall}''	Total emitter wall heat flux
x	Axial position
Γ	Emission to primary electron ratio
Γ_{c}	Critical emission to primary electron ratio (space charge limited)
Γ_{r}	Reflection coefficient
$\Delta\phi_{\text{SH}}$	Modification of work function due to Shottky Effect
ΔV	Change in velocity
α	Temperature coefficient of the material work function
ϵ	Permittivity
ϵ_0	Vacuum permittivity
ϵ_{i}	Ionization potential
κ	Space charge-limited emission constant

μ	Permeability
ρ_e	Electrical resistance of LaB ₆
ϕ_0	Temperature independent work function
ϕ_c	Critical plasma sheath potential (space charge limited)
ϕ_s	Plasma sheath potential
ϕ_{wf}	Material work function
ω	Wave frequency
ω_p	Plasma frequency

Chapter 1

Introduction

1.1 Motivation and Background

1.1.1 Why do cathodes matter?

Since electric rockets were first space-tested in the 1960's [1], thermionic hollow cathodes have been a critical component of both Hall and gridded ion thrusters. Indeed, cathode performance strongly dictates the performance and life of both Hall and ion thrusters [2].

Today there are over 230 active spacecraft with masses greater than 100 kg using electric propulsion. About 30% of these spacecraft rely on Hall and ion thrusters using thermionic hollow cathodes [3]. Applications for Hall and ion thrusters range from station keeping to orbit raising for Earth-orbiting satellites and interplanetary travel for science missions.

The use of electric propulsion (EP) on commercial satellites is continually expanding in order to realize either greater payloads or dramatic weight savings, the latter potentially leading to a significant reduction of launch costs. Originally only used for station keeping, electric propulsion for orbit raising became a commercial option after unintentionally being proven viable when EP was used to help recover a satellite

from an inadequate orbit insertion [4]. In 2012 the Boeing Company started offering “all-electric” ion thruster-based spacecraft using only electric propulsion [5] (versus chemical-only or a hybrid of chemical and EP) and was followed by other spacecraft manufacturers soon after.¹ Although taking longer to start on-orbit operations, this greater utilization of EP allows for lower-mass satellites that can be launched on smaller but attractive low-cost launch vehicles, like the SpaceX Falcon 9.

For interplanetary spacecraft, the use of Hall and ion thrusters are popular and we expect this trend to continue based on the capability of these thrusters to efficiently deliver a large change in velocity (ΔV), recent successful science missions (Deep Space 1 [6], Smart-1 [7], Hayabusa [8], and Dawn [9, 10]), as well as mission-planning trends, e.g., the Asteroid Redirect Mission [11]. Due to the continued and expanding application of these electric thrusters, we expect thermionic hollow cathodes to remain a key subsystem technology the foreseeable future of space travel.

1.1.2 Why do we need better cathodes?²

State-of-the-art hollow cathodes used in Hall and ion thrusters have met most near-term solar electric propulsion and commercial satellite lifetime requirements through extended operational life tests and in-space operation near 50,000 hours (50 kh or about 6 years) [10, 13, 14]. However, previously proposed electric propulsion missions [15–17] to interplanetary destinations required lifetimes from about 60 kh to 120 kh (7 to 14 years). Any future missions proposing to reach to the outer planets of our solar system or other distant bodies will require similar EP thruster lifetimes.

In addition to the future need for extended lifetimes, power levels available for propulsion are expected to increase by an order of magnitude in the next few decades

¹Full disclosure: The author worked for the Boeing Company in 2011 and was involved in these all-electric efforts.

²This section has been adapted from Ref. 12: M. L. Plasek, C. J. Wordingham, S. R. Mata, N. Luzarraga, E. Y. Choueiri, and J. E. Polk. Experimental Investigation of a Large-Diameter Cathode. In 50th AIAA/ASME/SAE/ASEE Joint Propulsion Conference, 2014.

as extrapolated from recent trends in space power generation [18]. The U.S. Air Force Research Laboratory (AFRL) projects that next-generation electric thrusters will need to be capable of processing 100-200 kW of power, dwarfing the 0.5 to 12 kW range of focus of the previous decade [19]. At the specific impulse levels relevant to Air Force missions (between 2000-6000 seconds), this translates to roughly 300-700 A of discharge current—at least one order of magnitude higher than currents commonly used in electric thrusters today, e.g., the nominal 20 A for a 6 kW laboratory Hall thruster [20].

The National Aeronautics and Space Administration (NASA) continues to show strong interest in higher thruster powers. As summarized in Ref. 21, recent mission studies require spacecraft powers of 300-700 kW for human exploration using solar-powered electric propulsion. Above 500 kW of spacecraft power, individual thrusters utilizing greater than 50 kW are necessary.

Hall thrusters are being developed in the 20-100 kW power range which can require discharge currents up to 400 A [22]. For example, a 50 kW class Hall thruster has been developed at NASA and was tested up to 100 A of discharge current as reported in 2012 [23]. Both the AFRL and NASA supported the design and development of a 100 kW class nested-channel Hall thruster undergoing testing currently [18, 24]. We suggest referring to the 2014 doctoral dissertation of Florenz [18] for further argument on the need for high power EP thrusters (Florenz focuses specifically on the near-term use of nested-channel Hall thrusters). Other examples of high-power thrusters in different stages of development and testing include the ELF, a field-reversed configuration fusion thruster (potential for 10-100 kW) [25], magnetoplasmadynamic thrusters (tested up to 185 kW) [26], and the VASIMR VX-200 (tested up to 200 kW) [27].

A need that has become more prominent is the requirement of not only long lifetimes or high-current capability but a cathode that can offer *both* high-current capability and significant lifetime simultaneously. In 2014, NASA cited work towards

the goal of designing and testing cathode assemblies with current capabilities greater than 100 A while maintaining lifetimes longer than 20 kh [28]. In early 2015, a cited NASA goal was building a 250 A cathode with at least 15 kh of operational life [29]. The 100 kW class X3 Nested-Channel Hall Thruster previously mentioned exemplifies the need for higher performance cathodes explicitly designed to handle high discharge currents while simultaneously providing long operational lifetimes.

Progress towards high-current, long-lifetime hollow cathodes has been made by Goebel and Chu [30, 31] in testing a lanathanum hexaboride (LaB_6) bulk-emitting hollow cathode at up to 300 A of discharge current, with that same cathode providing an expected life of 10-20 kh at 200 A. Van Noord, et al. [32], at NASA Glenn describe the design and testing of a dispenser cathode operating at 50 A of discharge current with a predicted life of 100 kh. More recently, Kamhawi and Van Noord [33] tested a dispenser cathode with a new emitter configuration allowing for a predicted life of 30 kh operating at 100 A of discharge current. Even with these selected advances, the expected improvement needed over the next few decades demands novel cathode concepts that can feasibly approach both lifetimes up to 100 kh and discharge currents up to 700 A. Further discussion of the current state of cathode research will follow in Section 1.2.

The RF-Controlled Hollow Cathode is a proof-of-concept experiment that attempts to address these requirements by adding radio-frequency (RF) power to a high-current thermionic hollow cathode. In the context of the literature, the difference between the RF-Controlled Cathode (referenced in this thesis as the RFC Cathode) and other cathodes referred to as RF cathodes [34, 35] is that we are adding RF power to a high-current thermionic hollow cathode as opposed to only using the RF waves for ionization without an electron-emitting insert. Combining a thermionic hollow cathode [2] with the RF cathode concept [34] allows for a high-current source with the potential for a significant performance enhancement from the added RF

power, as discussed further Chapter 2. This unifying design has the potential to be attractive for high-power, long-lifetime electric propulsion applications by maximizing insert utilization while helping to minimize erosion from high-energy ions. Before fully introducing the RFC Cathode, let us start with the context of such a proof-of-concept experiment.

1.1.3 A glimpse inside hollow cathode fundamentals³

Hall and ion thrusters need an electron source or sources in order to ionize neutral gas and create plasma as well as to neutralize the exhausted ion beam. Thermionic hollow cathodes fulfill this need. By using a low work function electron-emitting insert exposed to a current-carrying plasma, thermionic hollow cathodes can sustain high discharge currents over 300 A, high electron current densities greater than 20 A/cm², and do so at relatively low voltages compared to vacuum electron sources. Indeed, this helps hollow cathodes operate for relatively long lifetimes at high currents. For an in-depth discussion on hollow cathode fundamentals, please refer to Goebel and Katz’s *Fundamentals of Electric Propulsion* [2].

Here we will briefly discuss the relevant, governing equation for thermionic electron emission from the insert, or emitting material, within a hollow cathode. The current density due to thermionic emission from a hollow cathode insert is given by the Richardson-Dushman Equation [37]:

$$J_{te} = A_0 T^2 \exp\left(\frac{-e\phi_{wf}}{kT}\right). \quad (1.1)$$

Due to significant experimental variations from the theoretical constant $A=120 \text{ A/cm}^2\cdot\text{K}^2$, an experimentally-found temperature dependence (Eq. 1.2) can be substituted into

³This section has been adapted from Ref. 36 and expanded: M. L. Plasek, B. Jorns, E. Y. Choueiri, and J. E. Polk. Exploration of RF-Controlled High Current Density Hollow Cathode Concepts. In 48th AIAA/ASME/SAE/ASEE Joint Propulsion Conference, 2012.

the Richardson-Dushman equation (Eq. 1.1) to form the modified current density equation (Eq. 1.3) where D_0 is material-specific [37].

$$\phi_{\text{wf}} = \phi_0 + \alpha T, \quad (1.2)$$

$$J_{\text{te}} = A_0 \exp\left(\frac{-e\alpha}{k}\right) T^2 \exp\left(\frac{-e\phi_0}{kT}\right) = D_0 T^2 \exp\left(\frac{-e\phi_0}{kT}\right). \quad (1.3)$$

A hollow cathode insert emits electrons via thermionic emission under the effect of an electric field. This electric field is generated by the internal plasma sheath and the external positively-biased cathode keeper, with the latter helping to ignite the cathode plasma during the startup sequence. Plasma outside the cathode also affects the electric field since the external plasma potential is higher than the internal plasma potential [2]. The applied electric field effectively lowers the material work function that emitted electrons must overcome as first described by Schottky [38]. The addition of the Schottky effect or field-enhanced thermionic emission can be incorporated into Eq. 1.3, resulting in Eq. 1.4:

$$J_{\text{te}} = D_0 T^2 \exp\left(\frac{-e\phi_0}{kT}\right) \exp\left(\frac{-e}{kT} \sqrt{\frac{eE}{4\pi\epsilon_0}}\right). \quad (1.4)$$

A hollow cathode uses an insert of a specific material composition to act as a low-work function emitter in order to achieve the lowest temperature possible for a given current density as seen from Eq. 1.4.

Hollow cathode performance is derived predominantly from the properties of the electron emitter material, the physical configuration of the cathode, and structure of the cathode plasma, the latter two of which are the primary concerns of this thesis.

For state-of-the-art hollow cathodes used on spacecraft today a sharp peak in the axial profile of the plasma density within the internal cavity corresponds to a small current “attachment” area or a current-carrying plasma “contact” area with the emit-

ter surface. This restricted current attachment area leads to high current densities and high temperatures within a limited axial depth inside the cathode [2, 39, 40]. Upstream of this dense-plasma region, the plasma density is not high enough to support significant thermionic emission and so the emission is space-charge limited [20], as shown schematically in Fig. 1.1. Emitting significant electron emission from the full axial length of the emitter (e.g., 20 A/cm² for LaB₆) [37] requires that the profiles of both the plasma density and emitter temperature be “flatter” and uniformly greater than minimum values (for the above example, about 2×10^{19} m⁻³ and 1700 °C) [41] along the axial length of the emitter. When relatively uniform profiles are not possible, undesirable peaks in these axial profiles create regions that emit at higher temperatures and current densities, reducing the life of the emitter due to evaporation, while the remaining regions lack significant current density due to space-charge-limiting effects [20].

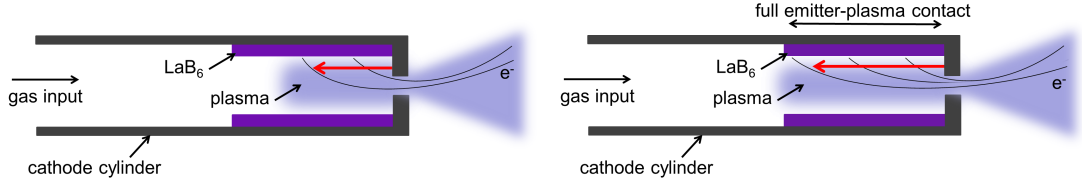


Figure 1.1: Side cutaway views of a basic hollow cathode showing the typical limited current attachment area along the length of the LaB₆ emitter (left) compared to the goal of current attachment to the full emitter area (right). The red arrow depicts the axial extent of the current attachment.

Approaching the ideally flat, uniform profiles of emitter temperature and internal plasma density allows the operator to choose some optimal balance between increasing the operational lifetime and increasing the discharge current to desired levels. This is the goal of adding RF power to a thermionic hollow cathode: to control or alter the axial profiles of plasma density and emitter temperature such that there is significant current attachment along the entire length of the emitter. In other words, we want to use RF power to alter the internal plasma structure so as to utilize the entire insert.

1.2 A Brief Review of the Recent Literature⁴

1.2.1 Methods to Increase Life and Discharge Current

There has been significant effort to date, documented in the recent literature, towards improving the operational lifetime and maximum discharge current of thermionic hollow cathodes. We provide a limited overview, focused on relatively recent developments, to explain the context of the RFC Cathode concept and design.

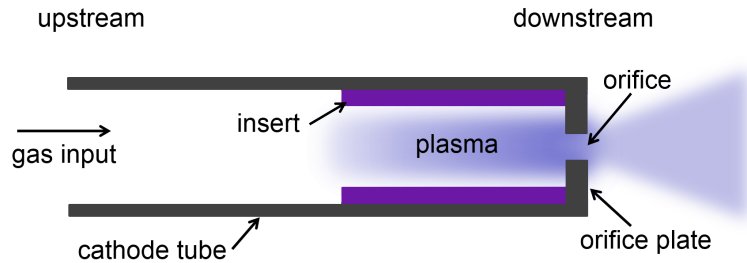


Figure 1.2: Side cutaway view of a typical thermionic hollow cathode setup.

In 2005, Van Noord, et al. [32] discussed the results of increasing the thickness of the hollow cathode walls in the emitter region in order to increase thermal conduction and decrease the temperature variation along the hollow cathode's major axis. Less temperature variation along the emitter insert leads to a more uniform emission and corresponding "flatter" plasma density profile. Although increasing the thermal conduction along the emitter region showed improvement in the length of the current attachment area [32], this can lead to a trade-off with required heater power. Generally, thinner walls and longer cathode tubes have minimal thermal conduction upstream of the emitter and therefore are desired for lower required heater power [22, 42].

Van Noord, et al. [32] proposed a second method to lower the peak current density and hence to allow an increase in the maximum discharge current. This method

⁴This section has been updated and adapted from Ref. 36: M. L. Plasek, B. Jorns, E. Y. Choueiri, and J. E. Polk. Exploration of RF-Controlled High Current Density Hollow Cathode Concepts. In 48th AIAA/ASME/SAE/ASEE Joint Propulsion Conference, 2012.

relies on increasing the emission area by increasing the insert inner-diameter. A cathode designed following these methods reached a predicted lifetime of 100 kh at 50 A of discharge current [32]. Goebel, Watkins, and Jameson [37] showed in 2007 that hollow cathodes of larger sizes can generally achieve longer lifetimes. These authors compared three different sizes of similar lanthanum hexaboride hollow cathodes (differentiated by their insert outer-diameters of 0.8, 1.5, and 2.0 cm) and predicted a lifetime of 100 kh at 75 A for their 2.0 cm diameter cathode [37].

In 2010, Goebel and Watkins [42] found that as the orifice diameter (or opening at the downstream end in Fig. 1.2) is increased the axial plasma density profile broadens and the area of the current attachment increases. The authors noted [42] that increases in discharge current and gas flow rate push the peak plasma density towards the orifice. In a small-diameter orifice cathode such as the NSTAR discharge cathode [43], pushing the plasma density peak towards the orifice leads to a narrowing of the plasma density profile and decreased current attachment to the emitter. In comparison, current attachment to the full emitter area was maintained by the large-diameter orifice cathode tested in Ref. 42. The predicted lifetime of the large-diameter orifice cathode was 100 kh at 20 A of discharge current or 10 kh at 45 A [42].

Goebel and Watkins [42] also noted that an increase in LaB_6 insert thickness could lead to a longer lifetime with lifetime roughly estimated from the bulk emitter evaporation rate. Assuming electron emission is not hindered over the life of the emitter, a bulk emitter has the advantage of a larger possible reservoir of emitting material compared to typical dispenser cathodes.

We note that both the beginning-of-life and the predicted end-of-life insert inner-diameters must be considered when selecting an insert thickness. To a rough, first-order estimate, insert thickness is a trade-off between cathode lifetime limited by emitter evaporation and the emitter area available to reach a desired discharge current.

In 2011, Goebel and Chu [22] developed and tested high-current LaB_6 cathodes having 1.5 and 2.0 cm insert outer-diameters and cathode tube lengths between 6 and 15 cm, depending on the application. In their case, the orifice was sized to 80% of the inner insert-diameter and significant plasma density extended beyond the upstream end of the insert [22]. Hence, increasing the length of the insert and selecting a relatively large-diameter orifice would decrease the current density and increase expected lifetime. For even longer lifetimes, Goebel and Chu [22] suggested a larger diameter cathode, as noted previously [32].

The 1.5 cm insert outer-diameter cathode from Ref. 22 had a predicted lifetime of 12 kh at 100 A discharge current, whereas the 2.0 cm cathode’s lifetime was predicted to be 20 kh at 200 A based on the assumption of evaporation-limited lifetimes [22]. These cathodes were constructed from graphite tubes for testing. As reported in 2014 [31], a more durable version of the 2.0 cm cathode was made from a molybdenum tube and has been tested up to 300 A of discharge current. This cathode was later integrated into the X3 Nested-Channel Hall Thruster and successfully operated at up to about 200 A of total discharge current demonstrating that LaB_6 cathodes can reach high currents in operating conditions [18].

The authors cited in this review [22,31,32,37,42] have proposed changing the physical dimensions and properties of the typical hollow cathode tube design to achieve longer lifetimes and lower current densities at a given discharge current. These design improvements include: increasing thermal conduction along the emitter while minimizing conduction away from the emitter region, increasing the thickness of a bulk-emitting insert, increasing the insert inner-diameter and length, and increasing the orifice diameter. In addition to these lifetime-improving design recommendations, to raise the maximum discharge current, again the insert dimensions must increase to provide a larger emission area, assuming a fixed utilization percentage of the emitter

area. In summary, following these recommendations for achieving longer lifetimes and larger maximum discharge currents requires increasing the size of the cathode.

Increasing the cathode and insert size can be difficult for geometry-constrained thrusters and impact already tight configurations. An example of a geometry-constrained application is the internally-mounted (or centrally-mounted) hollow cathode for Hall thrusters. The internally-mounted cathode configuration has been shown to increase total Hall thruster efficiency, lower thruster plume divergence and increase plume symmetry [15, 44, 45]. Two high-power examples of internally-mounted cathodes are the NASA 457Mv2 [28] and the X3 Nested-Channel Hall Thrusters [18, 24].

Since an internally-mounted cathode is located in the center of a Hall thruster annulus, the cathode length is the only relatively unconstrained dimension. A high-current cathode constrained in the nested-channel Hall thruster case would need a larger length-to-diameter ratio to provide enough emitter surface area for high discharge currents of greater than 300 A. Such a cathode is likely to be space-charge limited at some upstream depth even with the aforementioned design recommendations followed as possible within constraints. Controllable RF power absorption near the upstream emitter region could prove to be a method of flattening the plasma density profile so that no part of the longer insert is space-charge limited assuming the insert inner-diameter is not sufficient to reach the maximum discharge current.

1.2.2 Energetic Ion Mitigation and RFC Cathode Relevance

With an increased orifice diameter to extend current attachment, the internal neutral gas pressure is lowered and the axial plasma density profile benefits by becoming broader and more uniform. However, the combination of a low cathode gas flow rate and a large-diameter orifice can reduce the cathode neutral pressure enough to induce a transition from quiescent “spot” mode to a large voltage-oscillation “plume”

mode [46, 47]. Plume mode occurs when the neutral pressure is too low for a given current and is defined by significant supply voltage or plasma potential oscillations. Plume mode is linked to the production of high-energy ions that can critically erode the cathode keeper end plate and cathode orifice region by ion sputtering, causing off-design operation and eventual failure as shown in life testing. The literature also has shown that energetic ions become more prevalent at higher discharge currents in what is called “jet” mode [46–50].

Further study is underway to understand the fundamental mechanisms behind high-energy ion production [29, 51]. Whether in concert with plume mode or high discharge-current operation, reducing the number and energy of these damaging ions can be done by increasing the gas flow rate for a given cathode design [47, 49, 51, 52]. Unfortunately an increased gas flow rate can decrease the overall efficiency of a thruster by a few percentage points [49]. Increasing the gas flow rate is an undesirable solution related to our long-lifetime discussion in particular as increasing the gas flow rate pushes the plasma density peak towards the orifice, thus decreasing the current attachment area and cathode life.

In 2007, Goebel, et al. [47], introduced a new method for reducing energetic ions by injecting cold gas into the cathode plume immediately outside of the cathode assembly. The external gas injection allows the internal cathode gas flow rate to be reduced without entering plume mode. Since the internal gas flow rate can be decreased, internal neutral pressure is lower and the current attachment is broader. From this result, the authors noted that a majority of the gas flow through a cathode is not necessary for processes inside the cathode but is actually required for the production of sufficient current-carrying plasma *outside* the cathode [46, 47].

In 2012, Goebel, et al. [20], demonstrated that the gas flow fraction for the cathode (typically 7-10% of the total thruster gas flow rate), can be reduced to lower levels (5% or lower) without entering plume mode. This lower internal gas flow rate resulted

in current attachment broadening. The authors [20] showed that without this broadening, a drop-off in plasma density can cause the electron emission along the insert to become space-charge limited at some distance from the orifice. For example, if their insert length is increased and the gas flow rate is decreased as suggested, plume mode could be avoided while the predicted life their insert would be increased by four times [20].

External gas injection and the effects on high-energy ion production were studied in more detail by Chu, et al. [52], in 2013. They found that at a high discharge current of 250 A even a significant external gas flow rate of 20 SCCM⁵ (at 16 SCCM internally) did not reduce the high-energy ion production enough to extend the predicted keeper life beyond 2000 h. Even with higher internal and external gas flow rates, another method to greatly reduce or eliminate high-energy ion erosion is needed for discharge currents greater than 300 A. Goebel, et al. [49], noted that judicious use of materials with low sputtering yields helps to treat the symptom of energetic ions, however does not address the source of high-energy ion bombardment. High currents greater than 300 A will require further study to reduce energetic-ion erosion as a lifetime limiting factor.

In summary, increased gas flow rates both internal to the cathode and externally reduce energetic ion production in all cases. The highest reduction of eroding ions has been shown to result from the highest gas flows tested to date. Of course, although higher internal gas flows reduce energetic ion erosion, they also restrict the current attachment area and reduce the life of the emitter. The RFC Cathode is a possible answer to extend the current attachment area even at higher internal gas flow rates, thereby giving the best solution for long life both in terms of increasing emitter lifetime and minimizing erosion due to energetic ions.

⁵SCCM is Standard Cubic Centimeters per Minute, meaning mass flow rate of a neutral gas at standard temperature and pressure.

1.3 Thesis Objectives and Organization

There has been significant advancement in the field of thermionic hollow cathodes for EP thrusters in the last two decades. Although many practical improvements and fundamental insights have been gained, cathodes are still a limiting component of many EP thrusters in terms of maximum discharge current and operational lifetime. We look towards the requirements of the next generation of EP thrusters as cathode performance has historically been outpaced by thruster development needs.

Our current cathode research effort aims to discover novel cathode concepts that can demonstrate the potential to achieve order-of-magnitude improvements in lifetime and maximum current over the current state of the art. One of these novel concepts selected for consideration is the RF-Controlled Hollow Cathode, a thermionic hollow cathode in which RF power is added.

The driving purpose of this ongoing research is based on the following primary question:

Can we control the internal plasma structure of a thermionic hollow cathode by adding RF power in such a way so as to increase the cathode's operational lifetime and maximum discharge current?

This thesis documents the research we have done in pursuing this question and leads us up to the initial operation of the RFC Cathode experiment. Although we have not yet arrived at a conclusive answer the above question, a valuable subset of inquiry germane to this thesis is the following:

What are the challenges of scaling the inner diameter of a thermionic hollow cathode significantly larger?

We proceed to consider these questions in Chapter 2, where we start by identifying potential configurations of the RFC Cathode concept and select a configuration for experimentation based on discussed parameters. Next we support the viability of

the concept with computational numerical modeling in Chapter 3. Then we lay out the details of the RFC Cathode Experiment, including relevant design decisions, the experimental setup, methods, and diagnostics, before to reporting our experimental results of operating a large-diameter cathode in Chapter 4. Finally, in Chapter 5 we identify critical areas of development and recommend next steps for both the RFC Cathode and large-diameter cathodes in general.

Chapter 2

Concept Exploration and Design

2.1 Conceptual Design¹

The appeal of the RF-Controlled Cathode is that the concept has the potential to be an attractive solution for high-power, long-lifetime electric propulsion applications by maximizing insert utilization while helping to minimize erosion from high-energy ions. The potential benefit of maximizing insert utilization and lifetime is achieved by maintaining a lower maximum current density than without RF power while maintaining the same discharge current. We hypothesize that by adding energy via RF waves to the upstream insert region, the axial plasma density profile and corresponding plasma attachment area can be controlled or manipulated. If the RF power absorption instigates a change in plasma properties over a significant distance (on the order of centimeters), the absorption could broaden the plasma attachment area and increase the corresponding flattening of the plasma density profile by adding energy to produce a similar plasma upstream, as described in Chapter 1. For cathodes operating in a regime where the plasma density falls off and emission becomes space-charge limited at some upstream location along the emitter insert, broadening the

¹This section has been adapted from Ref. 36: M. L. Plasek, B. Jorns, E. Y. Choueiri, and J. E. Polk. Exploration of RF-Controlled High Current Density Hollow Cathode Concepts. In 48th AIAA/ASME/SAE/ASEE Joint Propulsion Conference, 2012.

plasma attachment will enlarge the emission area and thus reduce current density at a constant discharge current [20].

2.1.1 Selection of an Emitter Insert Composition

High current density hollow cathodes can be broadly separated into two types: dispenser and bulk emitter cathodes [2]. Of dispenser cathodes, the most common “Type S” is composed of barium calcium aluminate impregnated into a porous tungsten matrix with a work function of 2.06 eV. These barium-oxide dispenser cathodes sometimes contain other refractory metals to further reduce the work function (“mixed metal matrix” cathodes). Adding scandium to produce a scandate-barium oxide-tungsten emitter results in even lower work functions as small as 1.7 eV. Dispenser cathodes require chemical reactions to enable a low work function. This dependence means dispenser cathodes are easily poisoned by impurities such as oxygen and water in the propellant or the environment that can drastically raise the effective work function. Despite this drawback, dispenser cathodes have lower work functions than bulk emitters and thus require lower temperatures to sustain a given current density [2].

Due to these low work functions, dispenser cathodes have been the primary emitter of choice for ion thrusters manufactured in the United States [53]. In contrast, Russian-made SPT Hall thrusters have used lanthanum hexaboride (LaB_6) bulk emitter cathodes, with hundreds flown since 1971 [22]. The first U.S. reported use of LaB_6 for hollow cathodes was by Goebel, et al. [2], in 1978. More recently, NASA’s Jet Propulsion Laboratory has developed high current LaB_6 cathodes for high power Hall thrusters [2, 22]. Since 2004 LaB_6 cathodes have also seen commercial use by U.S.-based Space Systems/Loral[©] in SPT-100 Hall thrusters [54].

The use of LaB_6 bulk emitter has spread to the U.S. due to the emitter’s ability to strongly resist poisoning in comparison to dispenser cathodes, despite the higher 2.67 eV work function of polycrystalline LaB_6 [2]. LaB_6 is the emitter material itself

and does not require any chemical reactions to maintain its low work function. LaB_6 also resists other forms of failure affecting dispenser cathodes [2]. In spite of the higher temperatures required of LaB_6 to achieve the same current density as a dispenser cathode, simulations using lifetime models have shown that LaB_6 actually achieves a longer life due to a lower evaporation rate below around 15 A/cm^2 and more bulk emitting material available for the same size as compared to dispenser cathodes [22, 37]. For comparison, tungsten has an order of magnitude higher evaporation rate than both dispenser and bulk emitter cathodes up to current densities of 30 A/cm^2 [37].

Due to strong resistance to poisoning, longer simulated life, and demonstrated ability to reach high current densities above 20 A/cm^2 (at $\sim 1700 \text{ }^\circ\text{C}$) and high currents up to 300 A [20], we chose LaB_6 as the emitter for testing our cathode concept.

2.1.2 Two-Stage Configuration

One implementation of the RFC Cathode concept relies on adding an RF power transfer pre-stage to a typical LaB_6 cathode, shown in Figure 2.1. An RF antenna would be embedded in, or encircle, a pre-stage section made of a dielectric like a refractory ceramic. A pre-stage with a dielectric wall would allow the RF waves to pass through ceramic cylinder while maintaining a high temperature barrier between the internal plasma and the antenna. Refractory metals or graphite are commonly used [2] for the cathode cylinder and are opaque to electromagnetic waves due to their significant electrical conductivity. RF power would be added in the pre-stage immediately upstream of the second stage emitter insert as shown schematically in Figure 2.1.

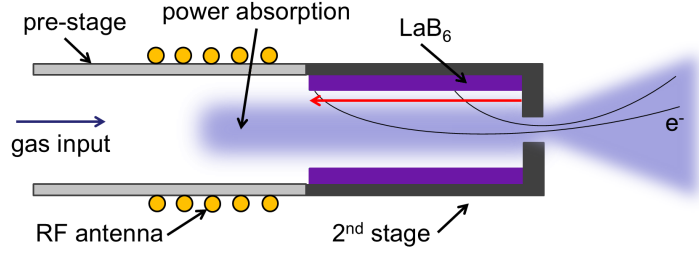


Figure 2.1: Two-stage configuration of the RFC Cathode LaB_6 hollow cathode with the dielectric pre-stage on the left, encircled by a RF antenna. RF power is deposited near the upstream insert region, inside the pre-stage. The red arrow depicts the axial extent of the current attachment.

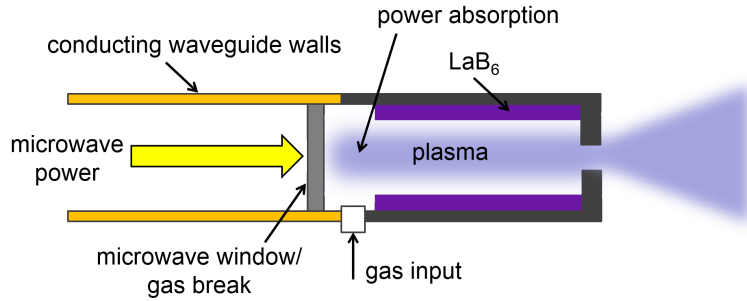


Figure 2.2: Single-stage configuration of the RFC-Cathode LaB_6 hollow cathode with the upstream end mated to a circular waveguide. RF power is deposited in the plasma near the upstream insert end after traveling through the microwave window.

2.1.3 Single-Stage Configuration

Another configuration of the RFC Cathode, depicted in Figure 2.2, is a single-stage device where a subset of RF waves at higher frequencies (1-40 GHz range), or microwaves, are injected upstream of the cathode and intended to propagate downstream, along the cathode major axis to the plasma attachment region. This configuration mates the upstream end of the cathode to a microwave source via a waveguide and effectively treats the conductive cathode cylinder as a cylindrical waveguide. Gas enters the cathode after a dielectric gas break in the waveguide which prevents back flow. The major difference between the two-stage and single-stage configurations is that the single stage is named such because RF power is deposited within the in-

sert region or stage, as opposed to a farther upstream region as in the two-stage configuration.

A waveguide mating can be used if the microwave frequency is above the cylindrical waveguide cutoff frequency, $f_{co, wg}$. A cylindrical wave guide allows prediction of the location of greatest magnitude electric field from a Transverse Electric (TE) or Transverse Magnetic (TM) wave mode and can be impedance matched with common tuning mechanisms, e.g., a triple stub tuner [55, 56].

Electron Cyclotron Resonance (ECR) heating was considered but the high frequency required to meet the TE_{11} mode cutoff in the baseline cathode geometry also requires a magnetic field approaching 0.5 T for resonance. This magnetic field strength is well above common magnetic fields used in ECR and is difficult to reach with the thermal characteristics of the system (e.g. Curie temperature of permanent magnets). For our analysis, we are interested in the location of strongest electric field as this is where most of the RF energy is expected to be absorbed by the plasma through heating, and where breakdown would occur if RF is used as an ignition source [55].

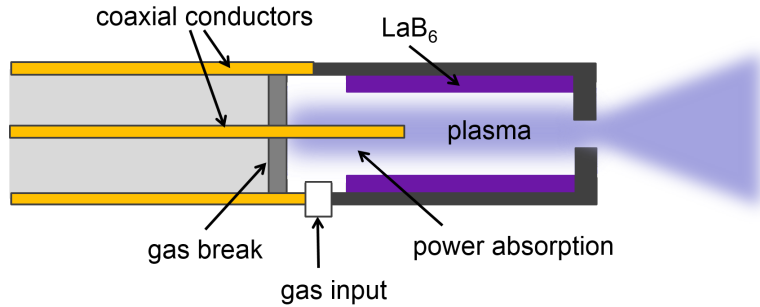


Figure 2.3: Single-stage configuration of the RFC-Cathode LaB_6 hollow cathode with the upstream end on the left, mated with a coaxial cable. RF power arrives from the left where power is deposited in the plasma near the upstream insert end.

If a lower frequency source is preferred due to expense or availability, it is possible to use a coaxial cable mating to propagate a Transverse ElectroMagnetic (TEM) wave into the cathode cylinder as depicted in Figure 2.3, a variation on the waveguide

single-stage configuration. A wave frequency below the cylindrical waveguide cutoff frequency, $f_{\text{co,wg}}$, will not propagate in the cathode once two conductors are no longer present (where the inner conductor ends), but this configuration will still allow the energy to be absorbed into the a region cathode plasma at low microwave frequencies. A coaxial cable can also be used at wave frequencies higher than $f_{\text{co,wg}}$ for a flexible connection between the source and cathode. Staying below the coaxial cutoff frequency ($f_{\text{co,coax}}$) allows only a TEM mode to propagate without interference from TE or TM modes. Coaxial cable dimensions can be selected to carry a microwave source frequency, f_{source} , able to meet the needs of a given microwave source and desired cathode mating [55]. In order to propagate a TEM wave mode with minimal interference in a coaxial line and transition into propagating a TE or TM mode in a cylindrical cathode waveguide, it is required that:

$$f_{\text{co,wg}} < f_{\text{source}} < f_{\text{co,coax}}. \quad (2.1)$$

Ideally, we want the microwave energy to be so fully absorbed in the emitter region as to produce no reflections. To achieve this, the cathode must be seen as a dummy load by the incident microwaves. A dummy load would be perfectly impedance matched and would absorb all of the transmitted wave power from the microwave source. In practice, impedance matching can be difficult with an impedance-varying plasma and so a manual tuning device is appropriate [56].

We also note that a microwave source requires a potentially life-limiting cathode for electron emission. Various space-qualified microwave sources (e.g. Traveling Wave Tube Amplifiers or TWTAs) use cathodes that have lifetimes which extend beyond the stated hollow cathode lifetime goal of 100 kh as tested [57,58] Microwave source thermionic cathodes with lifetimes >100 kh are usually mixed metal matrix

cathodes and can achieve such lifetimes due to relatively low operating temperatures (<1000 °C) and low current densities ($1\text{-}2$ A/cm²) [57].

2.1.4 Comparison of Configurations

For a proof-of-concept experiment, the RF power efficiency is not a primary concern, though a high enough percentage of power needs to be absorbed by the plasma in order to warrant the additional system complexity of an RF source. A challenge of the two-stage configuration is ensuring that enough power from the RF antenna is transferred to the cathode without requiring an unreasonable amount of antenna input power. The mismatch between the characteristic RF antenna wavelength, which is on the order of 10 m for a source frequency in the MHz range, and the dimensions of the pre-stage cylinder (around 1-10 cm) would lead to low expected energy coupling [55].

Another related challenge is material thermal limitations. An embedded antenna would give the greatest amount of radiated power to the pre-stage as the distance between the pre-stage and the antenna is minimized. However, if the antenna is in thermal contact with the pre-stage, high temperatures and a resulting high impedance should be expected. In contrast, the antenna could be thermally isolated and actively cooled. Thermal isolation and cooling would allow for greater antenna input power, but at the cost of increased distance from the target which would lower the amount of radiated power available to the pre-stage. As a thermal advantage, a dielectric pre-stage would likely be less thermally conductive than the typical refractory metal or graphite, and would allow for less heat loss and a decreased heater power level to reach cathode ignition temperature.

The single-stage configuration solves the challenges related to having the RF waves introduced from outside of the cathode by directly mating a waveguide or coaxial cable from a microwave source to the upstream end of the cathode cylinder. This results in a minimal loss of wave energy before the high-frequency RF waves (mi-

crowaves) are introduced into the cathode. However, the single-stage comes with its own set of complexities. The mating of the cathode and waveguide or coaxial cable requires matching diameters and materials in such a way as to minimize impedance mismatches. For the coaxial mating variation, a DC break must be incorporated into the inner conductor of the coaxial line to separate RF and DC circuits since the cathode will be kept at a voltage bias. A gas break of appropriate thickness that can manage plasma contact and is transparent to microwaves (e.g., boron nitride) must be fitted into the waveguide or coaxial cable at an appropriate depth.

Sputtering of the inner and outer conductors of the coaxial line, or of the waveguide after the gas break, may need to be addressed. At microwave frequencies (1-40 GHz) the ions are too massive to have much response in the short time scale before the electric field switches orientation, so even for coaxial potential differences in the hundreds of volts, significant ion sputtering of the antenna is not expected to be dramatic. We also note that LaB_6 cathodes have insignificant internal ion sputtering due to an internal plasma potential of less than 15 V [22]. If noticeable erosion does occur, the conductors of the waveguide or coaxial cable could be insulated with a ceramic, like alumina, which is a common insulation for RF antennas that are exposed to ion sputtering [2]. However, if the conductor or gas break material is redeposited on the insert, than this would be a critical drawback negating any life extension if the problem could not be remedied.

The single-stage configuration has the key advantage of minimal input-power loss compared to the two-stage configuration. Similarly, using a waveguide to transfer microwave energy over the distances considered (>2 m in our experimental setup) will transfer much more of the initial power to the actual cathode than with coaxial cable losses at high frequencies. Therefore, we have selected a single-stage waveguide configuration (Fig. 2.2) for further study in both numerical modeling and for our RFC Cathode experiment.

In the interest of unambiguous continuity and relying on the broad definition of radio frequency, we refer to this configuration as an RF-Controlled Cathode (or RFC Cathode) and use “microwave” and “RF” interchangeably though we refer to the same incident frequency.

2.2 Selected Design Considerations²

The goal of the RF-Controlled Hollow Cathode is to expand the axial extent of the current attachment such that the emitter area operating in a thermally-limited regime is maximized, and, consequently, space charge-limited emission is minimized. In high current density hollow cathodes, space charge-limiting prevents the full utilization of the emitter which directly limits the cathode operational lifetime and the maximum discharge current [2].

A minimum plasma density is needed to support a given electron emission current density. The maximum electron current density that a plasma can accept due to space charge-limiting effects at the emitter wall [2] is given by

$$J_e = \frac{\kappa}{2} n_i e \sqrt{\frac{kT_e}{m_e}} \approx \frac{1}{4} n_e e \sqrt{\frac{kT_e}{m_e}}. \quad (2.2)$$

Equation 2.2 tells us that space charge-limiting effects require that plasma densities greater than 10^{18} m^{-3} must exist in the cathode in order to reach an appreciable current density of around 2 A/cm^2 at the emitter as shown in Figure 2.4. Plasma densities on the order of 10^{19} m^{-3} are required to reach more substantial current densities that are no longer space charge limited and instead have transitioned into the thermally-limited regime. However, upstream plasma densities on the order of 10^{18} m^{-3} will still result in increased emission compared to a typical cathode config-

²This section has been adapted from Ref. 41: M. L. Plasek, C. J. Wordingham, and E. Y. Choueiri. Modeling and Development of the RF-Controlled Hollow Cathode Concept. In 49th AIAA/ASME/SAE/ASEE Joint Propulsion Conference, 2013.

uration with insignificant upstream plasma densities (e.g., the NSTAR cathode [13]). For a lanthanum hexaboride (LaB_6) bulk-emitting hollow cathode, thermally-limited current densities are typically greater than 20 A/cm^2 corresponding to an emitter temperature of about $1700 \text{ }^\circ\text{C}$ [2].

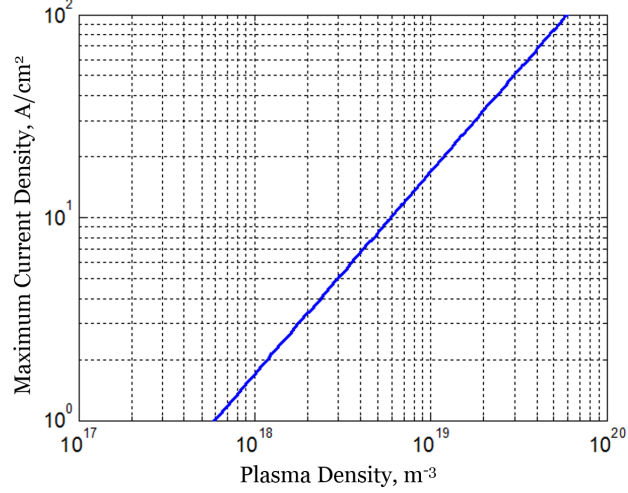


Figure 2.4: Maximum electron current density at the emitter wall as a function of plasma density. Argon gas and an electron temperature of 1 eV are assumed.

2.2.1 Adding RF Power to a Thermionic Hollow Cathode

Achieving the necessary plasma densities in an upstream, RF-generated plasma depends on the frequency of the RF source. Typically, the maximum plasma density generated is related to the incident RF excitation frequency; at a critical plasma density, the corresponding plasma frequency is equal to the excitation frequency and the RF waves begin to be reflected. Due to this reflection, the maximum plasma density generated generally does not greatly exceed the incident excitation frequency [35].

The RF frequency is also a major driver of the cathode design, and trade-offs between higher- and lower-frequency sources include waveguide size, source cost, and source availability. The RFC Cathode configuration we analyze in this thesis mates a

waveguide to the upstream end of the cathode, effectively treating the cathode tube as a cavity or a continuation of the waveguide. Since the cathode is treated as a waveguide, the cathode diameter is determined by the waveguide cutoff frequencies, which describe the ability of the RF waves to propagate inside the waveguide without being reflected or converted into modes outside the dominant transverse electric (TE₁₁) mode. The lower cutoff frequency for a TE₁₁ mode in a circular waveguide [59] is given by

$$f_{\text{co}} = \frac{X'_{11}}{2\pi a \sqrt{\mu\epsilon}}, \quad (2.3)$$

where $X'_{11} = 1.841$ and a is the cathode inner radius in meters. From Equation 2.3 we see that a larger cathode radius a gives a lower cutoff frequency f_{co} . Applied to reasonable cathode diameters, the waveguide cutoff frequencies constrain the source frequency to the microwave portion of the RF spectrum.

Cost, mass, and availability of microwave sources differ widely, both for lab experimentation and for use in a space environment. Higher frequencies at the output powers of interest generally correlate with higher system costs and lower availability for a lab use. We selected a microwave frequency of 8 GHz as a compromise between the cathode/waveguide diameter, the RF source cost, and the effect on plasma density. As seen in Figure 2.5, a source frequency of 8 GHz corresponds to a critical plasma density of about $8 \times 10^{17} \text{ m}^{-3}$, near our minimum goal of the 10^{18} m^{-3} .

The input power also presents a compromise between minimizing the spacecraft power required to operate the additional RF subsystem and applying adequate RF power to achieve the desired result. Our incident RF power range of interest is ten to several hundred watts while the discharge power from thermionic emission is in the hundreds to thousands of watts assuming a discharge voltage of around 20 volts. Clearly, the added RF power is marginal relative to the power output from the thermionic emission current. The major contribution expected from the added RF

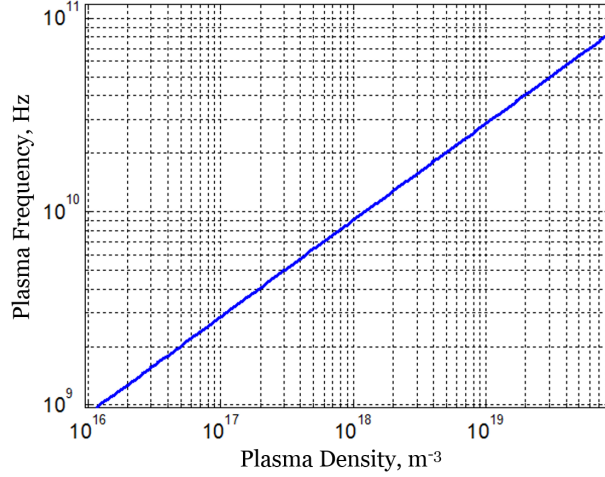


Figure 2.5: Electron plasma frequency corresponding to plasma density. A plasma density of about $8 \times 10^{17} \text{ m}^{-3}$ will reflect incident microwaves of 8 GHz.

power is to change the upstream cathode conditions in such a way that the overall thermionic emission is increased. The main processes by which this can occur are:

1. Increasing the plasma density in the upstream cathode to prevent space charge limitation, and
2. Increasing the upstream cathode emitter temperature via higher ion and electron bombardment rates, resulting in increased thermionic emission.

2.2.2 Cathode Size

Besides the addition of RF power, another unique feature of the RFC Cathode and its waveguide configuration is its inner diameter of 2.7 cm, which is approximately twice as large as any other cathode developed to date. The next largest hollow cathode we are aware of is Goebel and Chu's LaB_6 hollow cathode [20, 22] with an insert inner diameter of approximately 1.27 cm. For comparison, Goebel and Chu's [20] cathode can theoretically obtain approximately 400 A of discharge current from 20 cm^2 of

emitter area assuming a uniform emitter current density of 20 A/cm², while at the same uniform current density the RFC Cathode could achieve approximately 1360 A from its 68 cm² of emitter area.

The large diameter of the RFC Cathode is driven by the need for the diameter to contain the circular waveguide cutoff wavelength for an 8 GHz microwave frequency including a margin. In addition to analyzing the feasibility and behavior of the added RF power to a hollow cathode, we can also analyze the behavior of a significantly larger hollow cathode than those tested to date. A larger-diameter cathode is directly relevant to our stated goals and is a strategy suggested by many authors [32,37,42,60]. By using a larger diameter, and therefore a larger emitter area, we create the potential to achieve higher maximum discharge currents and lower current densities.

Other effects of a larger-diameter hollow cathode include lower operating pressures, less sensitivity to changes in neutral gas flow rate, and the need for higher flow rates to reach modest pressures. For example, using a one-dimensional Poiseuille flow model [2] the RFC Cathode is found to reach approximately 2 Torr along most of the axial emitter length from 70 SCCM of argon input assuming an orifice diameter that is 25% of the cathode inner diameter. In 2010, Goebel and Watkins [42] found that as the internal neutral gas pressure is reduced, the upstream depth of current attachment increases and the axial plasma density profile along the emitter length is flattened.

Another predicted effect is that a larger cathode will operate at lower temperatures [60] due to a shift in the power balance due to charged particle bombardment and microwave power deposition balanced with losses from thermionic cooling, thermal conduction along the cathode tube, and radiation from the surface. Lower emitter temperatures and decreased axial temperature gradients benefit the expected lifetime of the cathode. Assuming plume mode and the production of eroding ions can be avoided by using the appropriate orifice diameter, mass flow, and external injection

of neutral gas into the plume [30, 52], both a larger cathode diameter and added RF power are expected to increase the maximum discharge current while the lowering current density.

Chapter 3

Numerical Modeling¹

Before creating a time-intensive physical experiment, we used finite-element analysis to explore the RFC Cathode concept’s feasibility and qualitative behavior. Numerical simulations were performed with a simplified two-dimensional model which captures the internal cathode plasma, the LaB_6 thermionic emission, and the added RF power via upstream waveguide. In order to capture the upstream physical drivers but still maintain an approachable model, the orifice and related effects are not simulated. Due to these and other simplifications, we do not expect the simulation results to give quantitative agreement with experimental results. However, we do expect the key physical drivers in the upstream cathode region have been captured, giving an actionable indication of qualitative behavior.

3.1 Schematic and Computational Grid

The computational model we developed relies on a simplified version of the RFC Cathode, shown in Figure 3.1 below. The model used is two dimensional rather than

¹This chapter has been adapted from both Ref. 41: M. L. Plasek, C. J. Wordingham, and E. Y. Choueiri. Modeling and Development of the RF-Controlled Hollow Cathode Concept. In 49th AIAA/ASME/SAE/ASEE Joint Propulsion Conference, 2013. and Ref. 61: M. L. Plasek, C. J. Wordingham, and E. Y. Choueiri. Resonant Mode Transition in the RF-Controlled Hollow Cathode. In 33rd International Electric Propulsion Conference, 2013.

axisymmetric because of a known issue present in the microwave plasma model of COMSOL at the time of modeling.

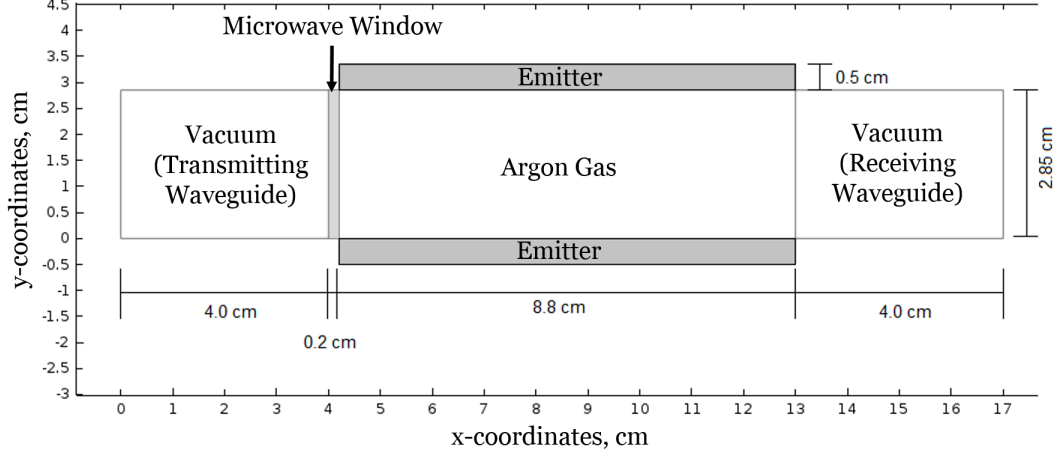


Figure 3.1: RFC Cathode Schematic Representation

We used the finite element method (with COMSOL software) and created a structured quadrilateral mesh with approximately 7000 domain elements as shown in Figure 3.2; this mesh was used for all simulations. After performing a grid sensitivity study by refining the grid by a factor of two in each node distribution, we determined that the grid shown offered the best balance of computation time and simulation accuracy. Simulation variables of interest, e.g. plasma density, varied by less than 2% when the grid density was increased.

3.2 Computational Model

The use of commercial software encapsulates functionality, reducing the time and effort required to create a working model, but also reduces the degree of customization

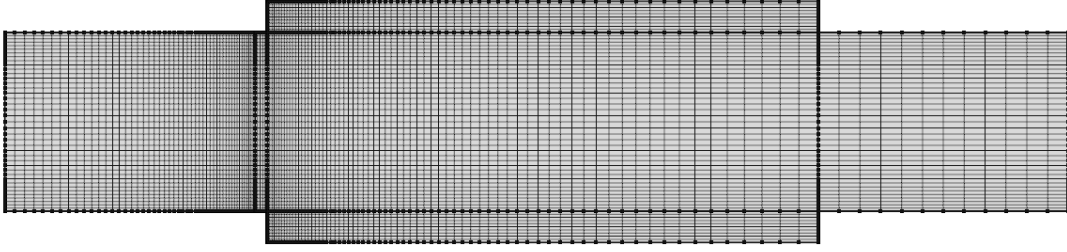


Figure 3.2: RFC Cathode Computational Grid, refined near regions of expected sharp transition, such as the plasma-surface boundaries and the microwave window.

available to the user. As such, the boundary conditions chosen are modified versions of those given in previous computational cathode studies [2, 62].

Flow and Neutral Pressure

In the computational model, argon gas is assumed to enter via the microwave window, which was found to be a good approximation because the simulation results were insensitive to the velocity field within the cathode (likely due to orifice exclusion). Having made this observation, we did not solve for the fluid velocity field. Instead, we model the effect of increasing argon mass flow by the dominant pressure determined using a Poiseuille flow model [2, 63] for an orifice diameter that is 25% of the cathode emitter inner diameter. The orifice itself is not contained in the model, and the plasma region modeled ignores effects due to the presence of an orifice, excluding its effect on the average neutral pressure.

Heat Transfer

Heat transfer within the cathode walls is solved for a stationary solution at each time step of the transient microwave plasma simulation (the heavy species temperature is assumed constant throughout the plasma). This solution method significantly reduces the total simulation time required for a steady-state solution. The outer boundaries of the emitter material are treated as radiative surfaces, approximating poor ther-

mal contact between the emitter and the cathode tube, and thermal conduction is restricted to within the emitter material. The inner boundaries of the emitter are in contact with the cathode plasma, and the heat flux into the emitter is determined using the plasma model detailed below. The combined heating and cooling due to the plasma fluxes and thermionic emission at the emitter wall is given by

$$q''_{\text{wall}} = q''_{\text{i}} + q''_{\text{e}} + q''_{\text{ex}} - q''_{\text{te}}, \quad (3.1)$$

where the heat flux due to de-excitation at the wall, q''_{ex} , was found to be negligible, and is excluded from further calculation. In addition to the plasma heat flux into the emitter, heating due to electrical conduction of the emitted current is modeled using a volumetric heat source,

$$\dot{q}''' = J_{\text{te}}^2 \rho_{\text{e}}, \quad (3.2)$$

where the electrical conductivity of LaB₆ is taken from a linear approximation of the temperature-dependent data given by Lafferty [64]. Finally, as shown in the schematic, the orifice region is ignored, but given the size of the RFC Cathode (limited by the waveguide properties required for the target RF source), the most prominent means of insert heating will likely not be orifice heating [2], but rather electron and ion impacts with the emitter.

Microwave Propagation

In our model, an input rectangular waveguide excited at the TE₀₁ mode provides RF power to the cathode via the microwave window. For a rectangular waveguide, the fundamental transverse electric (TE) mode is the TE₀₁ mode, but had we used an axisymmetric model we would have used the corresponding fundamental mode for a circular waveguide, the TE₁₁ mode. The inner cathode walls (including those of the emitter material) are considered to act as perfectly conducting surfaces for the

purposes of microwave propagation, but this assumption should have little impact on the results as microwave reflection and absorption within the plasma is the expected dominant means of attenuation. An exit waveguide is also included for the purposes of calculating microwave absorption in the cathode plasma.

Plasma Model and Wall Fluxes

Much of the plasma model, including the microwave power absorption, is encapsulated in COMSOL's microwave plasma model. In addition to the wall boundary conditions for the thermal model mentioned earlier, the plasma-contacting walls are set to a constant electric potential. The primary modifications to COMSOL's built-in model are comprised by the plasma heat flux coupling to the wall. The driving mechanism behind hollow cathode current generation is thermionic emission. Richardson's original work on the subject and its re-visitation by several other authors [65] eventually resulted in the Richardson-Dushman equation [2, 65]:

$$J_{te} = A_0 k_B T_w^2 \exp\left(\frac{-e\phi_{wf}}{k_B T_w}\right), \quad (3.3)$$

where the universal constant $A_0 = 120.17 \frac{A}{cm^2 K^2}$ is typically replaced by an experimentally determined constant, $D_0 = 29 \frac{A}{cm^2 K^2}$, where the value shown is that found by Lafferty [64] for lanthanum hexaboride. Because the thermionic emission from the insert is driven by the temperature of the emitter, the wall heat fluxes due to the plasma are of critical importance to our model. The fluxes used in our analysis are modified from previous modeling studies and expressed in the equations below. Equation 3.4 gives the heat flux to the emitter wall due to the ion flux [2],

$$q_i'' = J_i \left(\epsilon_i + \phi_s + \frac{1}{2} \frac{k_B T_e}{e} - \phi_{wf} \right), \quad (3.4)$$

which is comprised by the energy released during recombination (assumed to occur for all ions striking the wall), the thermal energy gained by the ions during their acceleration in the pre-sheath, the energy gained by the ions as they are accelerated through the sheath potential (whose approximation is discussed later), and the energy removed from the wall by the recombination electron. Ions are assumed to strike the wall at the Bohm velocity for the purposes of calculating the flux to the wall, and the number density is computed by COMSOL. The wall heating due to the electron flux is given by [2]

$$q_e'' = (2T_e + \phi_{wf}) J_r \exp\left(\frac{-\phi_s}{T_e}\right), \quad (3.5)$$

where J_r is the random thermal electron current density to the wall [2],

$$J_r = \frac{1}{4} e n_e \bar{c}_e, \quad (3.6)$$

and the electron density, n_e is evaluated in the plasma at the sheath edge. Since COMSOL already computes the electron density at the wall, this value is simply used instead and the exponential term that accounts for the sheath variation of the electron density in Equation 3.5 is dropped. Finally, the heat flux removed from the wall due to thermionic emission cooling is

$$q_{te}'' = J_{te} \left(\phi_{wf} + 2 \frac{k_B T_w}{e} - \phi_s \right), \quad (3.7)$$

which accounts for the energy removed from the emitter due to the work function and the average thermal energy of the electrons that escape the wall, which is twice the wall temperature in eV [65]. Equation 3.7 also adds the heat produced by the emission electrons being accelerated through the sheath, as the sheath is too small to be captured by our computational grid in COMSOL.

Sheath Model

In order to evaluate the expressions in the plasma model, we need an estimate of the sheath potential. Due to the cold electron emission at the wall, the sheath potential is reduced and possibly spatially non-monotonic. This is especially true in the limiting case of space charge-limited emission, which is likely to occur for the lower plasma densities in the range of consideration for the RFC Cathode. Our model for the sheath potential is from Hobbs [66], and is formulated for a floating wall, but the same effect applies for a fixed-potential wall (the reduction of the sheath potential due to the cold emission electrons emanating from the emitter wall). If we assume that the ratio of emission to primary plasma electrons is low ($\Gamma \ll 1$), the sheath potential would be approximated by

$$\phi_s = \frac{-k_B T_e}{e} \ln \left[\frac{1 - \Gamma}{\sqrt{2\pi m_e / M_i}} \right], \quad (3.8)$$

where Γ is the ratio of emission to primary electrons. This is unlikely to be the case at the thermionic temperatures considered, and therefore we make the opposite assumption. We assume that the wall emission is space charge limited, and that the ratio of emission to primary electrons takes on the following critical value [66],

$$\Gamma_c = 1 - 8.3 \left(\frac{m_e}{M_i} \right)^{1/2}, \quad (3.9)$$

which is approximately 0.97 for argon. This emission-to-primary-electron ratio results in a sheath potential given simply in terms of the electron temperature (extracted from the model's output):

$$\phi_c = -1.02 \frac{k_B T_e}{e}. \quad (3.10)$$

Using this approximation for the sheath potential, we can calculate the heat fluxes to the emitter wall for the RFC Cathode. Given that the grid element size is too large

to effectively capture the sheath, the average energy of the emitted electrons is set higher than that given by twice the wall temperature, as the sheath acceleration must also be considered. The value chosen for the thermionic electron energy was fixed at 3 V because a variable energy based on the sheath potential caused the simulation to become unstable. This effectively lumps the cold-electron sheath effects into the wall boundary itself. Finally, we note that the effect of the RF electric field on the sheath near the microwave window and the modification of the work function [38] due to the Schottky Effect, $\Delta\phi_{\text{SH}}$, are ignored.

3.3 Results and Discussion

The first goal of our modeling is to gauge the feasibility of creating a substantial effect on the internal cathode plasma by adding RF power. The second goal is to gain insight into the trends that emerge from the modeled physics by comparing the results of different simulated cases. We are concerned primarily with the relationships between parameters and to a lesser extent with the quantitative accuracy, which we approach from an order-of-magnitude perspective as we are using a simplified model without an orifice or external plasma coupling.

The feasibility of the RFC Cathode depends on whether the added RF power can significantly affect the internal cathode plasma. From our modeling we found three major effects that result from the addition of RF power:

1. With increasing RF power the plasma density increases over most of the emitter length,
2. Increasing the RF power causes the axial location of densest plasma region to shift upstream on the order of millimeters to centimeters, and
3. A nonlinear transition occurs in the plasma density, upstream electron temperature, emitted current, and RF power absorption which is dependent on the

neutral gas pressure, the phase of the incident electric field, and the incident RF power.

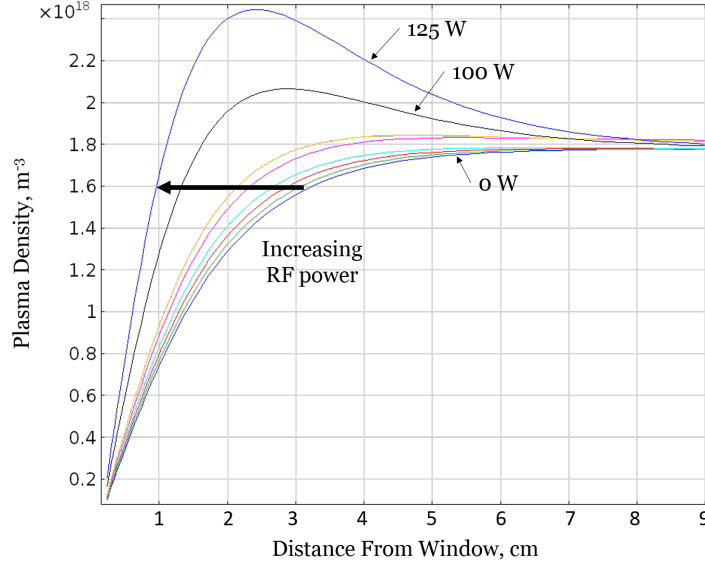


Figure 3.3: Plasma density profiles versus distance from the microwave window for a uniform pressure of 1.5 Torr (corresponding to an argon flow rate of 40 SCCM). As the RF power increases, a significant plasma density extends further upstream (shown by the bold arrow). The upstream microwave window edge is on the left (Distance From Window = 0 cm), while the downstream orifice is on the right (Distance From Window = 9.0 cm).

Let us start by examining our first two findings of the increasing plasma density and of the plasma density profile shifting upstream with increasing RF power input. Figure 3.3 shows the centerline plasma density profile along the emitter length for a uniform pressure of 1.5 Torr (200 Pa) corresponding to an argon flow rate of 40 SCCM (or 1.2 mg/s of argon). In Figure 3.3 we can see that the plasma density profile increases gradually for less than 100 W of RF power and shifts upstream with increasing RF power input. For example, at 3 cm from the microwave window with no RF power added the plasma density is $1.6 \times 10^{18} \text{ m}^{-3}$ and with 125 W of RF power input, the same plasma density shifts 2 cm upstream along the bold arrow to 1 cm from the window. Continuing the example, the original location at 3 cm increased in plasma density from $1.6 \times 10^{18} \text{ m}^{-3}$ at zero RF power to $2.2 \times 10^{18} \text{ m}^{-3}$ at 125 W RF

power while the location 1 cm from the window increased from about $0.7 \times 10^{18} \text{ m}^{-3}$ at zero RF power to about $1.7 \times 10^{18} \text{ m}^{-3}$ at 125 W. However, in the downstream region between 8 and 9 cm from the microwave window we can see there is little change in the plasma density profile due to the addition of RF power.

Although Figure 3.3 shows a beneficial increase and upstream shift in the plasma density profile, the figure does not include the aforementioned drastic transition behavior. This nonlinear transition in plasma density occurs at higher RF powers and is captured in Figure 3.4. We can see in Figure 3.4 that the plasma density preferentially increases about a peak at approximately 2.5 cm from the microwave window, corresponding to a peak in emitter temperature. The maximum plasma density increases by an order of magnitude to $4.7 \times 10^{19} \text{ m}^{-3}$ from an RF power increase from 125 to 150 W and the density continues to increase with RF power although only by about 30% over the next 200 W increase in RF input power. Even the region from 8 to 9 cm downstream of the window shows change, doubling in plasma density over the transition, although this is small compared to the maximum increase.

Figures 3.5 and 3.6 show similar plasma density profiles for a higher uniform pressure of 2.5 Torr (333 Pa), corresponding to an argon flow rate of 110 SCCM (or 3.3 mg/s). Similar behavior results, but we note that the transition is dependent on pressure; at this higher pressure the transition occurs between 20 and 30 W of RF power, much lower than the 125 to 150 W for a pressure of 1.5 Torr. This tells us that increasing RF power can decrease the cathode flow rate required to cause a nonlinear transition into a high-density operating regime. This high-density mode is beneficial as it significantly raises the space charge emission limit over most of the emitter area.

A two-dimensional representation of the same data from the 2.5 Torr cases without the transition can be seen in Figure 3.7 and a post-transition case at 2.5 Torr is seen in Figure 3.8. We note that the high-plasma-density region (for example, the region with plasma densities greater than $0.8 \times 10^{19} \text{ m}^{-3}$ colored in red) shifts markedly upstream

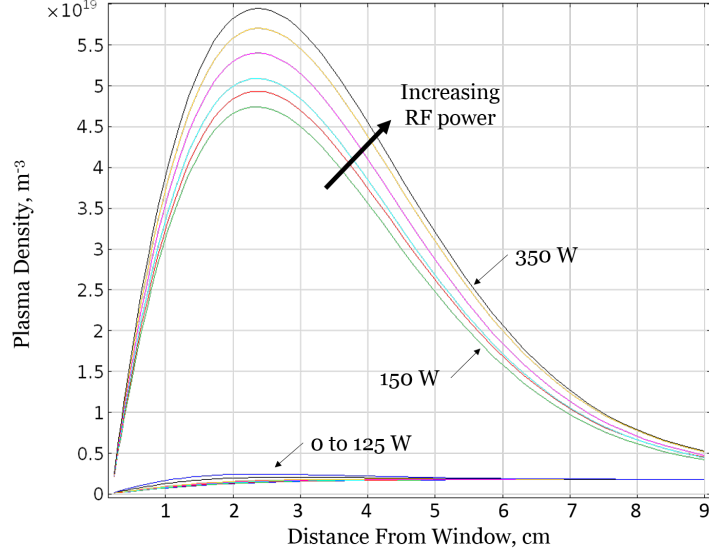


Figure 3.4: Plasma density profiles versus distance from the microwave window for a uniform pressure of 1.5 Torr (corresponding to an argon flow rate of 40 SCCM). As the RF power increases further, plasma density increases preferentially at the axial depth of the maximum plasma density and peak emitter temperature. The upstream microwave window edge is on the left (Distance From Window = 0 cm), while the downstream orifice is on the right (Distance From Window = 9.0 cm).

with increasing RF power from Figure 3.7a at zero RF power to 3.7c at 20 W of RF power. The centerline average and maximum plasma densities visibly increase as well.

We observed that the RF power absorption takes place over 1 cm or less from the microwave window before the RF power is reflected by the overdense plasma, undergoes further absorption in the 1 cm region, and then the remainder of the RF power travels back upstream creating a standing wave interference pattern. This power absorption increases the electron temperature in the same region but affects the entire plasma and the cathode's total thermionic emission. Therefore we suggest that the assumption that the greatest enhancement of thermionic emission and plasma density will occur in the region where the majority of the RF power absorption takes place, or the location of the highest incident electric field, is not an accurate assumption in a hollow cathode environment.

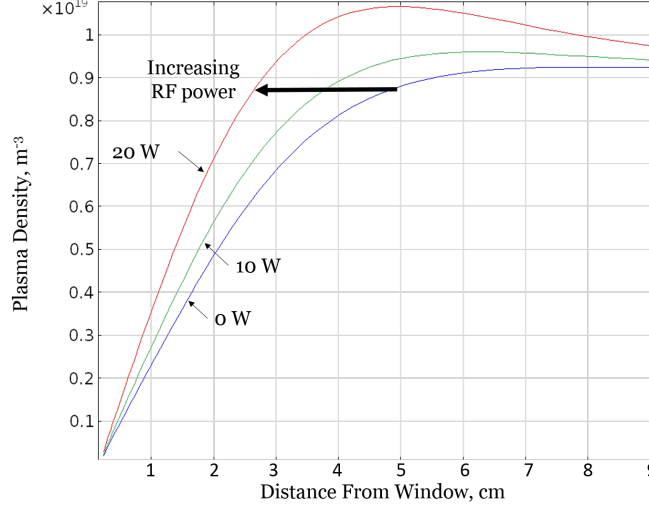


Figure 3.5: Plasma density profiles versus distance from the microwave window for a uniform pressure of 2.5 Torr (corresponding to an argon flow rate of 110 SCCM). As the RF power increases, a significant density extends further upstream (shown by the bold arrow). The upstream microwave window edge is on the left (Distance From Window = 0 cm), while the downstream orifice is on the right (Distance From Window = 9.0 cm).

We can qualitatively compare the zero RF power case in Figure 3.7a to other LaB₆ hollow cathodes [30] and find that the emitter temperature profile in our model also starts at a minimum temperature upstream and increases to the maximum value at the downstream end. Our modeling shows a slight temperature gradient in the LaB₆ emitter material at steady-state with the highest temperature corresponding to the location of the peak plasma density along the centerline. This behavior is expected due to greater thermionic emission rates from higher emitter temperatures as per Equation 3.3. Although effectively an estimation, the 1700 to 1800 K emitter temperatures from our modeling of the RFC Cathode are lower than those in other LaB₆ cathodes. Goebel and Chu’s [30] largest hollow cathode operates with an orifice (and assumed emitter) temperature greater than about 1800 K at its lowest measured discharge current (around 25 A). This temperature discrepancy is likely due to a combination of a simplified model that does not include orifice effects, the radiative thermal boundary conditions that can be varied substantially in our model and in an

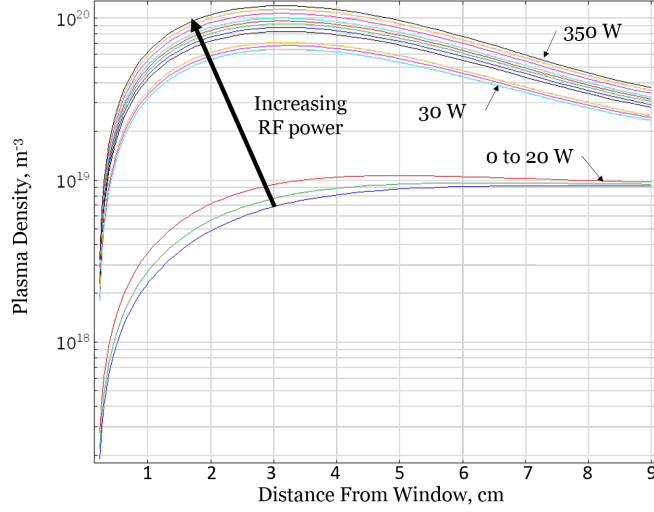


Figure 3.6: Plasma density profiles versus distance from the microwave window for a uniform pressure of 2.5 Torr (corresponding to an argon flow rate of 110 SCCM). As the RF power increases further, plasma density increases preferentially near the depth of the maximum plasma density. The upstream microwave window edge is on the left (Distance From Window = 0 cm), while the downstream orifice is on the right (Distance From Window = 9.0 cm).

actual experiment, and the RFC Cathode’s large diameter, which we expect to result in comparatively lower operating temperatures [60]. We also expect the peak plasma density to penetrate a significant depth upstream due to the large diameter and lower gas pressures present [2], and this behavior is seen in Figure 3.7a. The lower operating temperatures and the significant upstream penetration of a dense plasma are beneficial in reducing the peak emitted current density at a given discharge current.

Figure 3.8 is a continuation of the increasing RF power at 2.5 Torr from Figure 3.7. Figure 3.8 shows an order-of-magnitude increase in the maximum plasma density (using a different color scale than Figure 3.7) and a significant upstream shift in the peak of the density profile at an RF power input of 30 W. The emitter temperature has increased only marginally but shows a new trend in the temperature gradient; the temperature no longer peaks at the downstream end but more centrally, corresponding to the peak plasma density. The higher plasma densities that occur

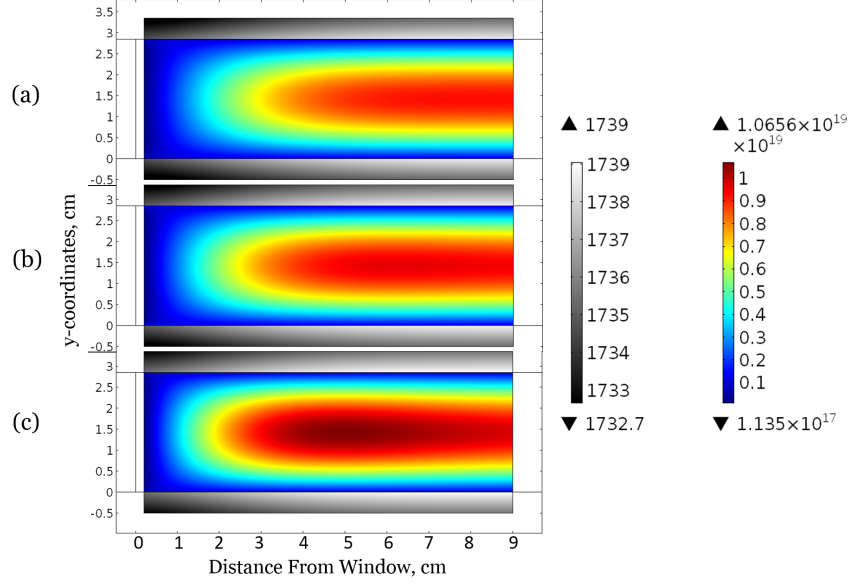


Figure 3.7: A two-dimensional representation of the plasma density profile versus distance from the microwave window corresponding to the curves in Figure 3.5. The three plots are using the same color scaling to compare increasing RF powers moving down with (a) 0 W, (b) 10 W, and (c) 20 W. Note that the centerline plasma density is increasing and the densest region moves upstream with increasing RF power. Surface plots of the emitter temperature are shown in grayscale above and below the plasma density surface plots.

after the transition, on the order of 10^{19} m^{-3} in Figure 3.8, meet our stated goal and allow current densities of 20 A/cm^2 .

We note that there is a peak in the plasma density's axial profile in the high density operating regime with the maximum density at least double that of the downstream minimum. This peak may result in a premature depletion of the emitter material at the location of the maximum plasma density, similar to the barium depletion observed near the downstream end in dispenser cathodes [43]. Considering that the simulated plasma density peak is much less sharp than that of the typical dispenser cathode [43], and that the current densities are much lower overall, we do not expect this to be a limiting factor in the lifetime of the RFC Cathode. With no added RF power the plasma density profile does not exhibit this peak and is relatively flat until it drops off upstream. This uniformity is nearly ideal, but does not take into account orifice

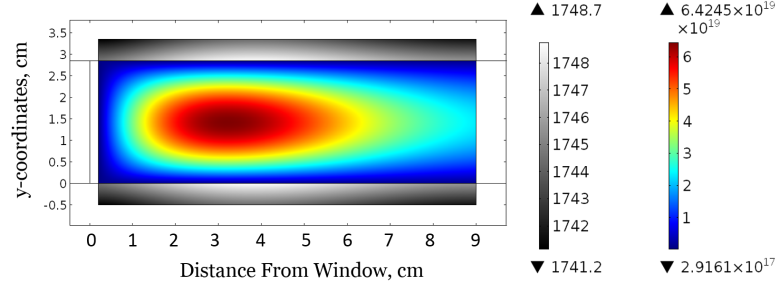


Figure 3.8: Continuing the increase in RF power from Figure 3.7, this two dimensional plot has an incident RF power of 30 W and has made a significant, sharp increase in plasma density. This figure has a different color scaling than the pre-transition plots in Figure 3.7. Surface plots of the emitter temperature are shown in grayscale above and below the plasma density plot.

effects. However, it is a reasonable approximation of an upstream cathode section for a large-diameter cathode.

3.3.1 Explanation of Nonlinear Transition Behavior

In the literature, we found both experimentally and theoretically observed phenomena similar to those uncovered in our modeling such as spatial shifts in plasma density [67, 68], abrupt jumps and increases in plasma density [68, 69], and overdense microwave-generated plasmas with power absorption taking place over a small skin depth [34, 67, 70]. Overall, our modeling results and simulated behaviors are qualitatively similar to experimental and numerical studies of microwave plasmas found in the literature [34, 67, 68, 70, 71].

Ganachev et al. [70], have shown that these behaviors can result from “surface waves” or microwave fields propagating along a dielectric-plasma boundary in thin tubes and in large-area plasma sources. Similar to surface wave behavior, our modeled plasma varies rapidly along the cathode’s major axis near the microwave window. Electron temperature spikes near the window from heating due to the incident RF waves, although only by a few tenths of eV over the insert-plasma averaged electron

temperature around 1.2 eV. We also observe an inhomogenous plasma that is sharply increasing in density downstream from the window boundary. After the transition, our plasma typically meets the plasma density criterion for surface waves $n_{\text{sw}} = n_c(1 + \epsilon)$ [70], where n_c is the cutoff plasma density corresponding to a plasma frequency equal to the incident RF frequency ($\omega_p = \omega$). In the RFC Cathode, using a boron nitride window, the surface wave criterion density is $4.0 \times 10^{18} \text{ m}^{-3}$. Although there is evidence that surface waves may contribute to a sharp transition under experimental conditions, we have ruled out surface waves as causing the observed transition as our two-dimensional numerical model (using COMSOL v4.3) does not account for fields propagating normal to the cathode major axis. We expect RFC Cathode behavior may vary in experimental testing from our numerical modeling due to the potential for surface waves to be present.

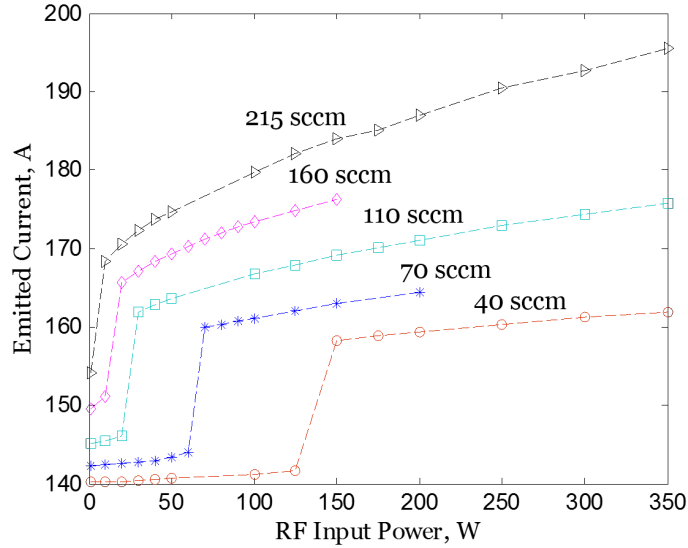


Figure 3.9: Emitted current versus RF power for five different flow rates corresponding to pressures used in our simulations. Note the clear increase in emitted current and the critical transition point's dependence on RF power and flow rate.

The nonlinear transition is shown for a variety of argon flow rates in Figure 3.9, where we plot integrated current emitted from the walls as a function of RF power. The emitted currents are seemingly low, but the operating temperatures we observed

are also notably low and correspond to the appropriate discharge currents. As noted above, the radiative thermal boundary conditions applied to the emitter may not correspond to experimental values and could offset the steady-state simulated temperature significantly.

The transition’s dependence on the gas pressure (therefore on flow rate and orifice size) and on RF power can be seen in Figure 3.9. We explored the behavior of the critical transition point and found that the transition is distinctly sharp and occurs over less than 1 W of RF power increase. However, we do not believe the transition is due to numerical instabilities as the model’s convergence near the transition is stable and predictable. Our model does not capture orifice effects or coupling to the external plasma, so we also do not expect the transition to be related to a plume-to-spot mode transition typically found in hollow cathodes.

Next in our analysis of the transition, we consider the location of the critical plasma density that reflects the incident microwaves. For 8 GHz this critical density is about $8 \times 10^{17} \text{ m}^{-3}$. Figure 3.10 shows an expanding plasma density contour of $8 \times 10^{17} \text{ m}^{-3}$ with increasing incident power. We can see that the contour expands to nearly the entire insert region and contacts the microwave window at the upstream end as the transition occurs. This corresponds to the RF power being reflected near the window-plasma boundary and RF power absorption taking place mostly within a skin depth ($\sim c/\omega_p$), which is a few millimeters from the window in our case.

Having observed the changes that the plasma undergoes during the transition, and a dependence of the critical transition RF power on waveguide length, we attribute the onset of the transition condition to a microwave cavity resonance that occurs within the cathode. As described previously, we observe that increasing the RF power added to a hollow cathode shifts the maximum plasma density upstream. Hence, the critical plasma density at which the incident RF waves are reflected also shifts upstream. This axially-moving critical plasma density effectively acts as a conducting wall of

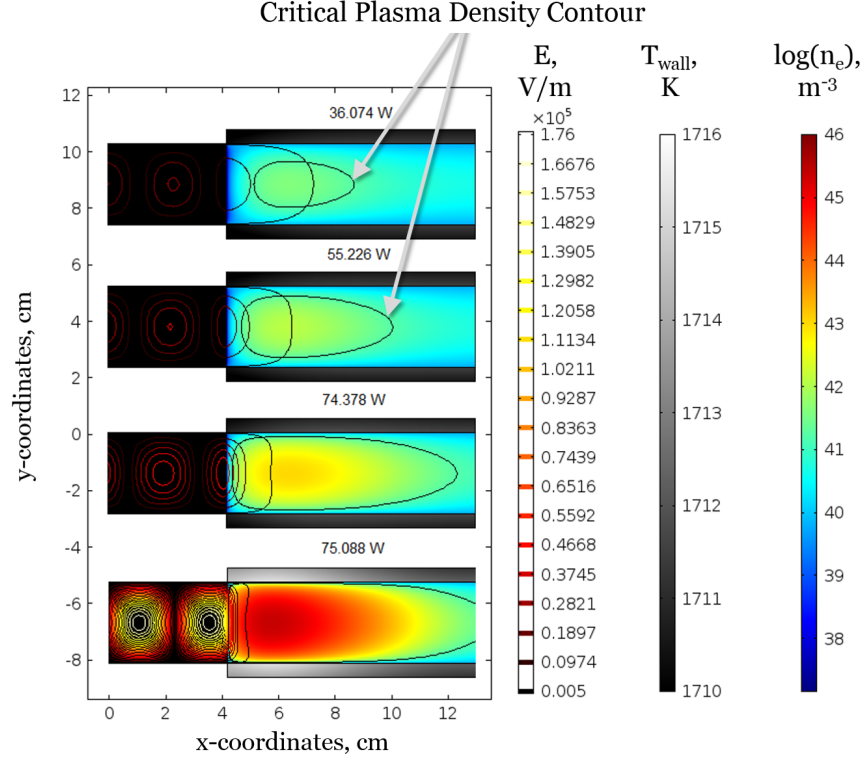


Figure 3.10: Progression of the critical electron density ($8 \times 10^{17} \text{ m}^{-3}$) contour with increasing RF power, showing the transition occurring as the critical density reaches the upstream window.

a microwave cavity and is “tuning” the cavity as the critical plasma density moves. The effective microwave cavity length formed by the critical plasma density depth and the RF input boundary decreases as the plasma density shifts upstream with increasing RF power. Given a sufficient phase shift of the RF electric field due to this decreasing cavity length and the appropriate input waveguide length (or appropriate input RF electric field phase), the cavity abruptly becomes resonant as the reflected and incident RF waves interfere in a solely constructive manner as seen in both Figure 3.10 and Figure 3.11. This resonance causes the RF electric field amplitude to abruptly increase significantly.

Moving to Fig. 3.12 let us first focus on the low reflection coefficient at very low RF powers ($< 20 \text{ W}$). This low reflection occurs at low powers because at lower

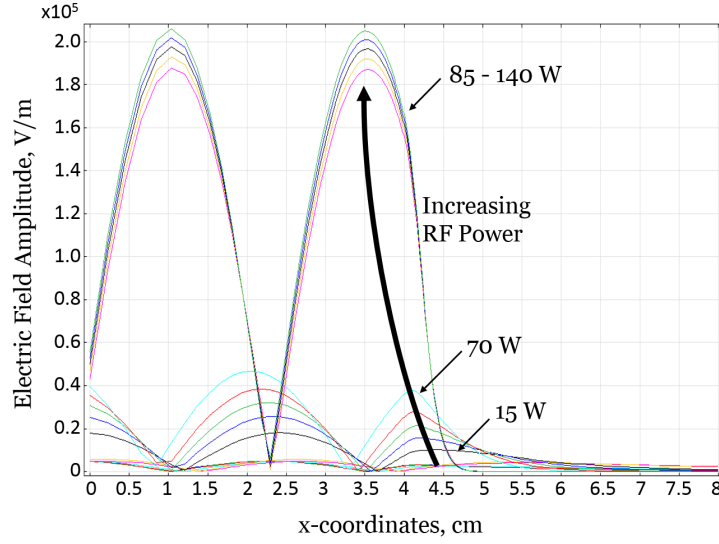


Figure 3.11: RF electric field amplitude curves for different RF powers as a function of waveguide position. At a critical RF power the electric field amplitude sharply increases in magnitude due to a cavity resonance condition. Note that the structure of the electric field amplitude changes significantly after the transition.

pressures (e.g., 1.5 Torr), the plasma is not dense enough to reflect a majority of the incident RF, i.e., $\omega_p < \omega$. For higher RF powers after the marked transition points, the plasma density increases, the skin depth decreases, and higher reflection results.

As we turn our attention to the clear transition points we see significant, sharp dips in the reflection coefficient Γ_r where $\Gamma_r = P_r/P_{in}$. For higher pressures these drops in Γ_r occur at lower incident RF powers and are more extreme. This behavior of the reflection coefficient at the transition signals a nonlinearly increasing “reduced electric field,” defined as E/n_0 , the ratio of field to neutral gas densities, corresponding to efficient RF power absorption [71]. Due to the resonant cavity effects at the transition, the electric field amplitude sharply increases as seen in Fig. 3.11. In addition, as more power is absorbed, the neutral gas density decreases due to ionization near the window, causing a pronounced increase in the reduced electric field as seen in Fig. 3.13 leading to a local spike in electron temperature [71] and an increase in

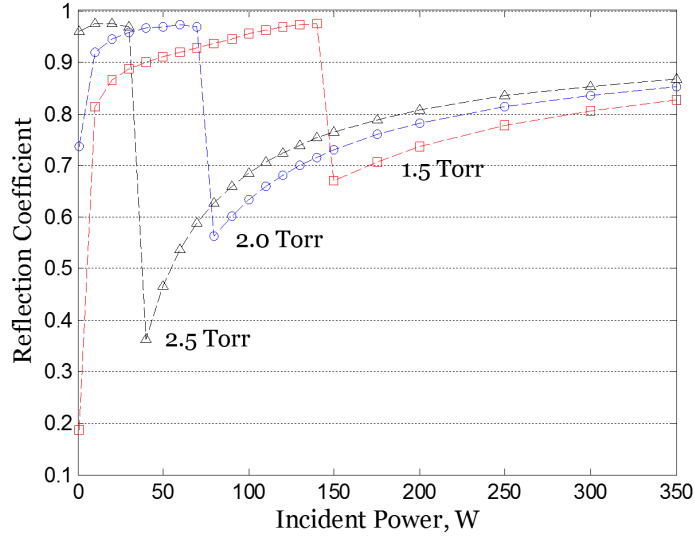


Figure 3.12: The reflection coefficient as a function of input RF power and pressure. Note the larger dip at the transition for higher pressures, corresponding to more efficient power absorption. At low RF powers and low pressure (1.5 Torr), the plasma density is below the critical density for RF reflection.

the plasma potential. The combination of the increased plasma density and particle thermal energies subsequently cause an increased heating of the emitter from enhanced electron and ion fluxes to the walls. The higher-temperature emitter emits increased electron current and the effect cascades downstream through the cathode. It is this described physical mechanism, starting with the resonant cavity mode and a nonlinear increase of the reduced electric field, that causes the abrupt transition we have observed in our numerical modeling.

3.3.2 Hysteresis and Post-Transition Stability

Microwave plasma sources have been shown to exhibit hysteresis [70], or plasma behavior dependent on a “memory” of its operational past. This means that the plasma can have multiple operating modes even at the same operating parameters depending on the source’s recent operating history. In the case of the RFC Cathode, we also found evidence of strong hysteresis, as shown in Fig. 3.14. The hysteresis in

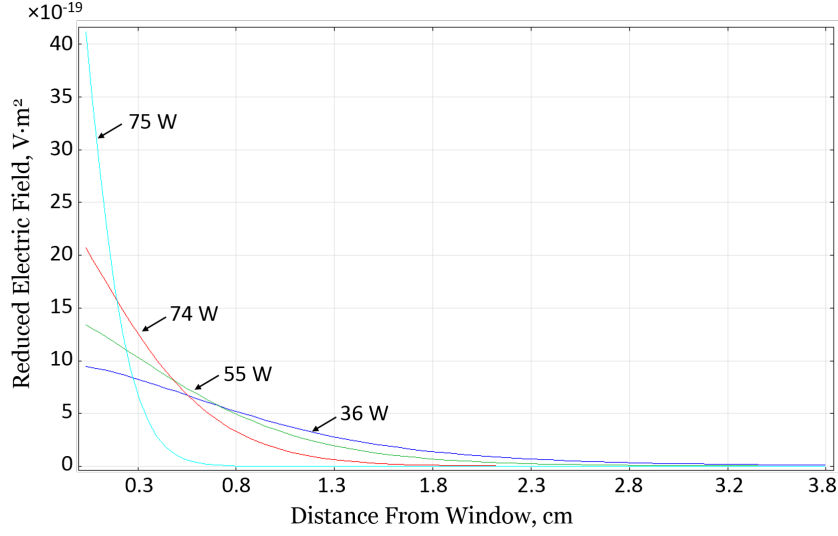


Figure 3.13: The reduced electric field amplitude E/n_0 for different input RF powers, with these four cases matching those in Fig. 3.10. The reduced electric field increases with RF power as the skin depth decreases.

Fig. 3.14 is expected to be indicative of experimental operation due to the slow change in RF power in our numerical simulation. However, for lower RF powers we anticipate some discrepancy with future experimental measurements as the simulation may not have reached steady state. Any significant amount of hysteresis in RFC Cathode operation will decrease the power budget requirement for increased lifetime and high-current operation.

The dependence of the transition on waveguide length (therefore on RF electric field phase) is shown in Figure 3.15. We note that the resonance repeats itself as the waveguide length is arbitrarily increased because of the repeating electric field phase and therefore a repeating resonance condition. Evidence of the repeating is shown in Figure 3.15, although, only one resonance is shown for simplicity.

After the transition, the upstream plasma density has reached a magnitude such that the incident RF wave is reflected at a minimum distance within the cathode, and further increases in RF power cause relatively small increases in peak plasma density, emission current, etc. We observe that further increasing the RF power does

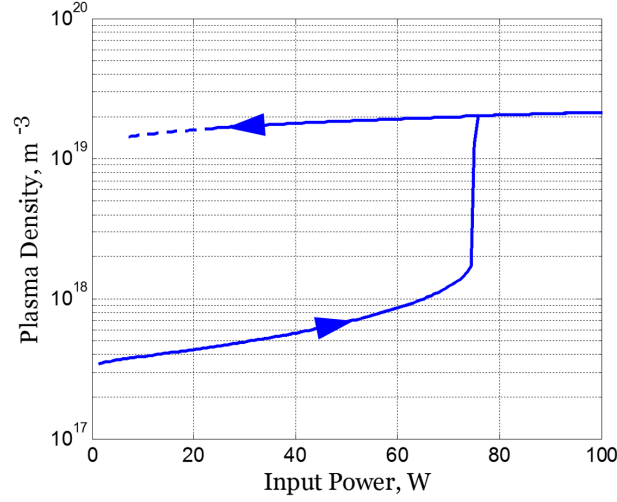


Figure 3.14: The average electron number density over the simulated emitter area is shown as a function of input RF power as the RF power is increased from 0 to 100 W and then slowly reduced to 0 W. The nonlinear transition behavior as the input power is increased and the hysteresis in the plasma density as the power is decreased are both evident. The low RF power range (< 20 W) of the upper branch may not have reached a steady-state solution.

not transition the cathode operation away from the cavity resonance as the resonance is maintained for all of the post-critical RF powers considered.

Therefore, according to these results, we would expect that once the transition has been made the cathode will operate in this post-transition regime for a wide range of RF powers, both higher and lower than the critical transition RF power.

3.4 Chapter Summary

From our numerical modeling we found that adding RF power to a cathode cavity does affect the internal plasma in several notable ways. Increasing the RF power leads to higher plasma densities over most of the emitter length and shifts the maximum plasma density location upstream along the cathode major axis. This behavior in-

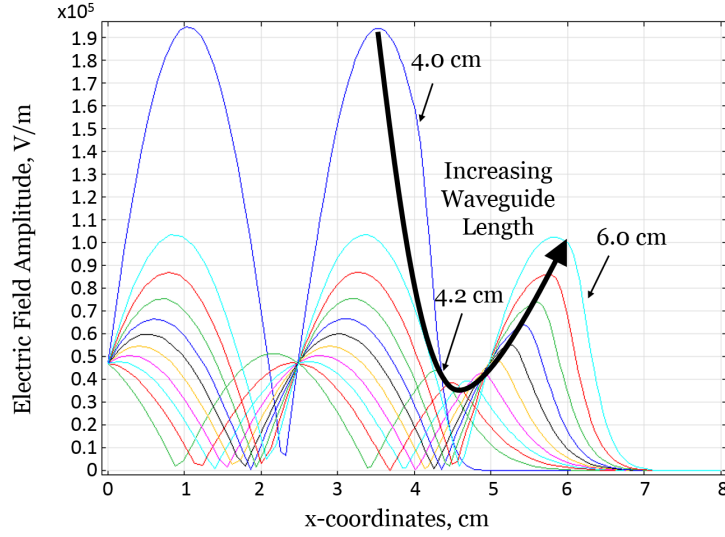


Figure 3.15: RF electric field amplitude curves for different waveguide lengths. At a critical waveguide length (4.0 cm in this case) for a fixed RF power (100 W), the electric field amplitude sharply increases in magnitude due to a cavity resonance condition. Note that the structure of the electric field amplitude repeats itself as the waveguide length continues to be increased.

creases the extent of dense plasma contact with the emitter and broadens the plasma density profile.

Our modeling results support that a large-diameter cathode, such as the RFC Cathode, improves expected operational lifetime by operating at lower emitter temperatures and increasing the upstream penetration of dense plasma contact. We expect that the RFC Cathode will reach plasma densities on the order of 10^{18} to 10^{19} m^{-3} along the entire length of the emitter resulting in desired thermally-limited emission for most of the emitter area.

We also found that a sharp nonlinear transition from a low- to a high-plasma-density mode occurs which is dependent on the internal neutral gas pressure (and therefore on flow rate and orifice size), the input RF power, and the incident RF electric field phase (or waveguide length). This transition results in a substantial increase in the incident RF electric field magnitude, absorbed RF power, and plasma

density. We found that an increase in the RF power can be used to reduce the required flow rate to reach the transition condition.

We have shown that the onset of the nonlinear transition is due to a microwave cavity resonance that occurs with the added RF waves. The critical plasma density at which incident RF waves are reflected is shifted with varying RF power, effectively creating a conducting cavity wall that moves axially to “tune” the RF electric field phase within the cavity. With the appropriate axial location of the critical plasma density, the incident and reflected RF waves constructively interfere to cause a sharp increase in the RF electric field amplitude. With an increased electric field amplitude, the ionization fraction increases and the reduced electric field increases sharply, signaling more efficient power absorption. With more power absorbed, this leads to a local increase in electron temperature and an increase in the plasma potential. These factors cause increased electron and ion fluxes to the walls further heating the emitter. The higher-temperature emitter emits increased electron current and the effect appears to cascade downstream through the cathode.

Numerically-modeled evidence informed by the literature support this physical interpretation of the transition and point towards significant beneficial hysteresis effects which suggest stable post-transition operation. In addition, surface waves may affect the experimental mode-transition behavior although their existence is not represented in our model.

The overall performance of the RFC Cathode is significantly improved both before and particularly after the observed nonlinear transition when evaluated against our stated goals of decreasing peak current density for a given discharge current and broadening the axial plasma density profile. The abrupt transition results in an increase of the maximum plasma density by an order of magnitude with a relatively low level of added RF power, which benefits the cathode’s operational lifetime and discharge current capability. In addition, we have substantiated the benefits expected

from a large-diameter cathode. In this chapter we have verified the feasibility of the RFC Cathode configuration from a first-order approach using numerical simulations and uncovered beneficial behaviors that merited an experimental investigation described in Chapter 4.

Chapter 4

Experiment¹

4.1 Design Features of the RFC Cathode

The large inner diameter of the RFC Cathode was driven by the need for the insert inner diameter to contain the circular-waveguide cutoff-wavelength of the selected 8 GHz microwave input frequency. The selection of an 8 GHz microwave frequency in the RF spectrum was derived from a trade-off study between the cathode inner diameter (acting as a waveguide), attainable RF plasma densities, RF coupling methods, and the cost and availability of an RF generator and amplifier. The resulting inner diameter of the RFC Cathode is 2.7 cm, which is approximately twice the inner diameter of any other LaB₆ hollow cathode developed to date. In addition to ease of selected microwave frequency input, the size of the RFC Cathode presents a unique opportunity to study the behavior of large-scale thermionic hollow cathodes.

In general, both a larger cathode inner-diameter [32, 42, 47, 60] and added RF power [61] are expected to increase the maximum discharge current while lowering current densities as detailed in Chapter 1. Next, we detail specific elements of the

¹This chapter has been adapted from Ref. 12: M. L. Plasek, C. J. Wordingham, S. R. Mata, N. Luzarraga, E. Y. Choueiri, and J. E. Polk. Experimental Investigation of a Large-Diameter Cathode. In 50th AIAA/ASME/SAE/ASEE Joint Propulsion Conference, 2014.

RFC Cathode design which impact the operation of a large-diameter bulk-emitting hollow cathode.

4.1.1 Novel Cathode Design

Figure 4.1 shows side-cutaway views of our RFC Cathode design that balances both RF and gas input in a high temperature environment. The press-sintered LaB_6 that comprises the emitter region, where the insert plasma is generated, is shown in purple. Depicted by the orange arrows in the second image in Figure 4.1, microwaves travel into the cathode tube (which is effectively a waveguide) and through a white disk made of hexagonal boron nitride. The disk serves both as a low-loss microwave window and a gas barrier in the cathode waveguide tube. We chose an axial disk thickness to be half of the incident wavelength (1.0 cm thick at 8 GHz) in order to maximize the transmittance.

Neutral gas is injected through the gray stainless steel base plate into an annular region between the two dark-gray graphite cylinders, where it travels downstream and then moves radially inward into the emitter region immediately after the microwave window. A two-dimensional view of this path is depicted by the light blue arrows in Figure 4.1. This novel gas injection scheme was used to prevent gas leakage into the waveguide portion of the cathode (potentially creating an unwanted plasma in the upstream waveguide) and to remove the need for costly and potentially problematic high-temperature brazes or welds on the downstream portion of the cathode.

We selected lanthanum hexaboride as an insert material due to its significantly higher poisoning resistance than typical dispenser cathode emitters, which allows for simplified handling and startup procedures [37]. LaB_6 as an emitter material also shows longer simulated lifetimes than dispenser cathode emitters [22,37], the ability to emit current densities above 20 A/cm² [37], and has demonstrated discharge currents up to 300 A [20]. In the RFC Cathode design, we selected an emitter insert length

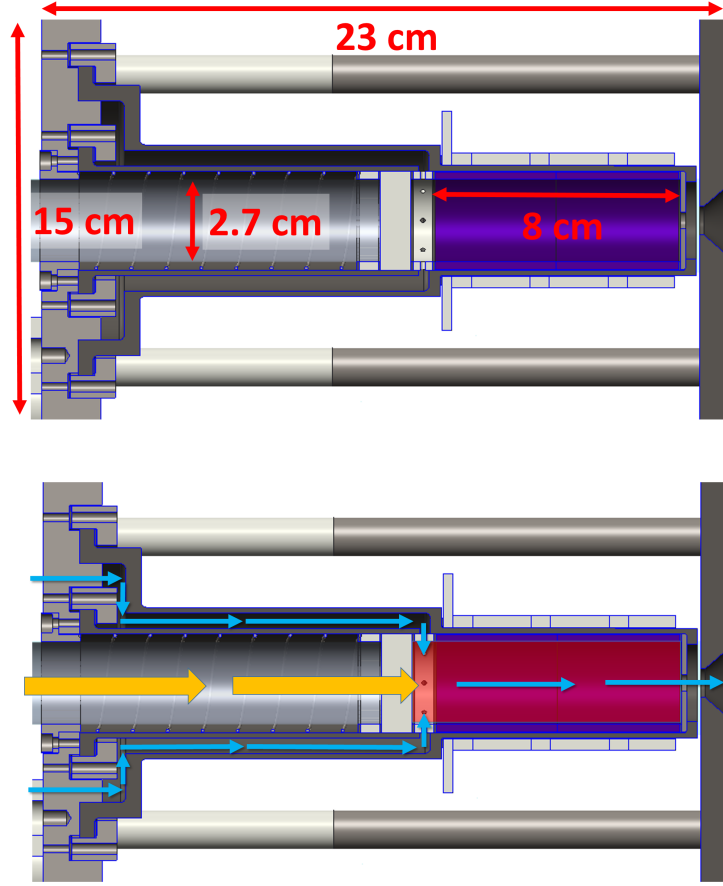


Figure 4.1: Side cutaway views of the RFC Cathode created in CAD software. The purple region in the top image is the LaB_6 emitter tube insert. In the bottom image, the orange arrows depict microwave propagation in waveguide, light blue arrows depict the neutral gas injection path, and the red overlay is the emitter region and internal cavity. Plasma exits downstream through the orifice to the right. The heater and heater radiation shielding are not pictured.

of 8 cm, significantly longer than seen in other large hollow cathode experiments (e.g., 5 cm) [52], so that we can more easily measure and discern the effect of RF input power on the axial profiles of plasma density and emitter temperature.

The RFC Cathode is significantly larger than previous large-cathode experiments and, as the cathode is a proof-of-concept experimental lab article only, we limited the keeper to a graphite disk suspended between the cathode and anode by stainless steel rods and ceramic stand-offs. By not entirely enclosing the cathode in a graphite keeper, we gained access to the outside tube surface of the emitter region

to place thermocouples and heater leads. This results in the RFC Cathode suffering greater radiative losses due to incomplete shielding. However, most of the radiation is reflected by three slotted molybdenum heat shields that are separated from one another to prevent thermal conduction. We electrically isolated the heat shields from one another to eliminate one significant source of arcing during operation, which was exacerbated by the sharp edges of the foil shields.

Heater

The heater is a critical element of a thermionic hollow cathode [72]. The heater is used to preheat the cathode’s emitter material to a temperature at which significant thermionic emission can take place and a cathode plasma can be ignited. For a large-diameter hollow cathode, losses increase substantially with the radius and the power input required to get to nominal operating temperatures is significant. For comparison, the typical heater power required to reach a peak axial temperature of 1450 °C for the RFC Cathode experiment is around 4 kW, versus 0.4 kW for the largest cathode reported by Goebel and Chu [30]. We expect that the heater input power could be lowered with better shielding, although retaining access to the cathode for measurements makes further shielding difficult. This power requirement could also be reduced by improving the heater design to increase thermal contact between the heater and cathode tube.

Due to the relatively high radiative thermal losses derived from the scale and shielding of the RFC Cathode as well as unoptimized thermal contact between the heater and cathode, depositing high power results in heater temperatures exceeding 1800 °C. This precludes the use of many high-temperature materials for heater insulation that are electrically insulating but retain significant thermal conductivity or degrade at these temperatures. As a first approach, we have used a bare tungsten wire as a resistive heater, but we have experienced problems including arcing, stable but

undesirable current attachment to the heater, embrittlement due to recrystallization, and undesirable chemical reactions with insulators at high temperatures. Specific electrical and physical heater details can be found in Section 4.2 with the results and operational description of our evolving heater design in Section 4.5.

4.2 Experimental Setup

Vacuum Facility

The RF-Controlled Cathode experiment was fabricated and tested in a fiberglass tank, 2 m in diameter and 5 m in length, which was evacuated to 6×10^{-5} Torr by two 0.0708 m³/s mechanical roughing pumps, a 0.632 m³/s roots blower and two 95 m³/s diffusion pumps. During cathode operation, the background pressure stayed in the high 10^{-5} to low 10^{-4} Torr range, and during measurements did not exceed 3×10^{-4} Torr, as measured by ionization gauges.

Cathode Configuration

An enlarged view of the emitter region of the cathode assembly is presented in Figure 4.2. The cathode components were all housed inside an 8.45 cm long graphite tube (grade AXM-5Q from Entegris/Poco Graphite). A lip on the downstream end of the tube held a tungsten orifice plate with a 0.56 cm diameter orifice. To prevent boron diffusion, a graphite foil “washer” (grade GTB Grafoil) separated this tungsten plate from the thermionically-emitting lanthanum hexaboride inserts (99.5% pure press-sintered from Materion). These inserts consisted of two 4 cm long, 2.7 cm inner diameter, 3.2 cm outer diameter tubes in contact with each other. Upstream of the inserts, we placed a boron nitride ring (all boron nitride is grade AX05 from Saint Gobain) in contact with the LaB₆. Six evenly-spaced radial holes were drilled into the boron nitride ring for gas input. Further upstream we placed a 1 cm thick

boron nitride disk (acting as a microwave window and gas break) and a second boron nitride ring to distribute spring pressure along the disk's edge, all separated with more graphite foil “washers.” The flexible graphite foil was cut into washer shapes that can compress and recoil. These properties allowed us to use the graphite foil as a seal to prevent gas flow upstream of the microwave window (or gas break). A tungsten spring wound in-house and placed upstream of the boron nitride pieces provided a force to keep all interior cathode components in place and in contact. Surrounding the outside of the graphite tube were six boron nitride insulating rings, three of which had 0.76 cm wide slots to allow thermocouple access to the cathode tube surface.

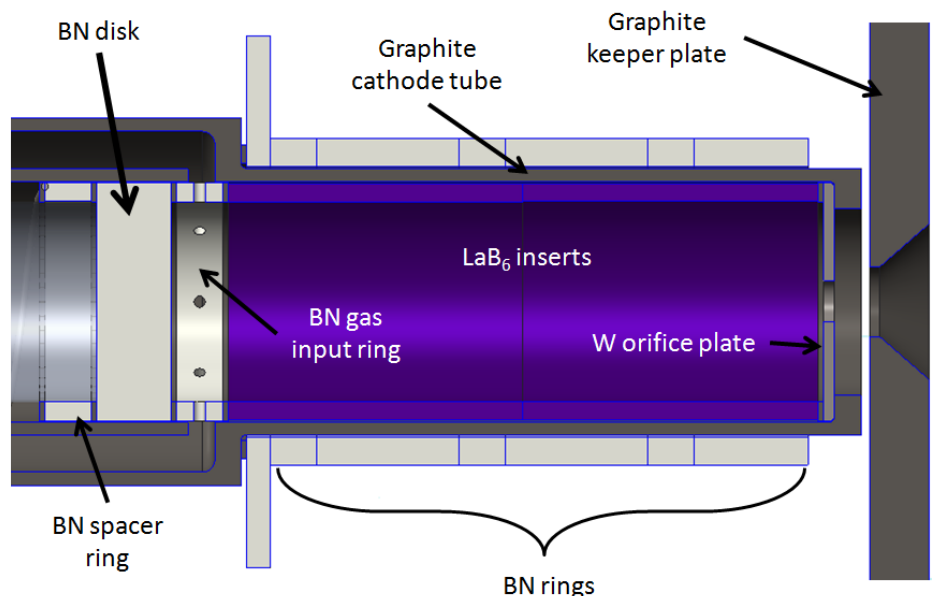


Figure 4.2: A side cutaway view of emitter region of the RFC Cathode.

A picture of the experimental setup installed in the tank is shown in Figure 4.3. We used a 2.5 turn bare tungsten wire for the heater which is wrapped around boron nitride rings for electrical insulation from the cathode. We also added graphite wire beads to stand off the heater wire from the boron nitride insulators, as will be discussed further in Section 4.5.2. The heater leads consisted of the heater wire along with many other similar-diameter tungsten wires tightly packed into an alumina tube

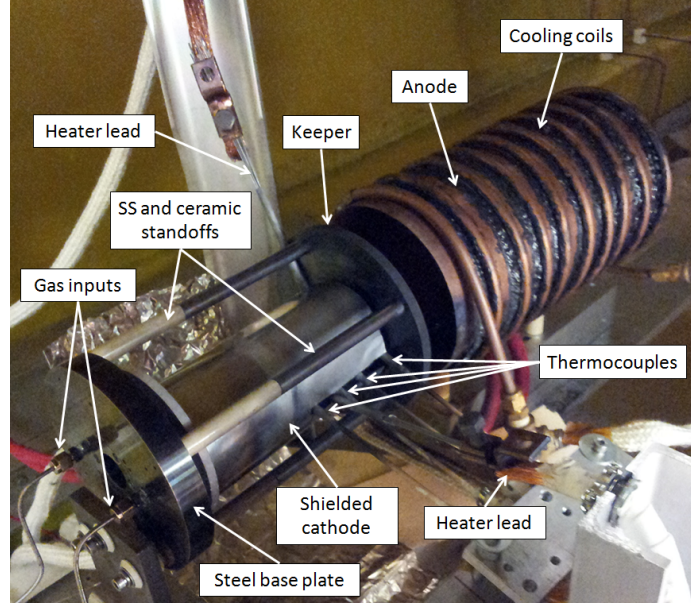


Figure 4.3: The RF-Controlled Hollow Cathode experiment installed in the tank.

for each of the two leads. This setup allowed for lowering both the electrical resistance and temperature of the leads due a larger effective cross-sectional area. Without the capability to weld tungsten wires together on-site, this heater lead design was a simple way to maintain a high-temperature electrical connection between the tungsten wires that could be disassembled easily. A copper wire lug was used to clamp the tungsten wires of each heater lead to an AWG 00 (2/0) copper welding cable.

Surrounding the heater were three electrically- and thermally-isolated 0.01 cm thick molybdenum sheet heat shields, with slots for thermocouples and heater leads. The graphite keeper plate, 15 cm in diameter and 0.79 cm thick, was placed in front of the cathode. The keeper orifice diameter was 0.96 cm with a 82 ° chamfer to a final downstream diameter of 2 cm. Four supports held the keeper about 0.13 cm from the downstream graphite edge of the cathode. Each support was a 12 cm long stainless steel rod connected to a 7.6 cm long ceramic stand-off. The steel end of each support was attached to the keeper while the ceramic portion was attached to the cathode baseplate for electrical isolation of the keeper.

The upstream edge of the anode was placed 3.8 cm downstream of the keeper plate. The anode was a 0.08 cm thick copper sheet rolled into a 15 cm diameter, 30 cm long cylinder with ten turns of a 0.95 cm inner diameter water cooling tube wrapped around the outside. A flexible mastic initially provided good thermal contact between the cooling line and the copper sheet. However, at higher anode currents, plasma interactions and localized anode spot heating rendered parts of the mastic inflexible and the cooling line lost full contact to the cylinder. Due to this reduced thermal contact, initial testing was limited to below 250 A as localized anode melting was witnessed at this high current level. Simply brazing the water line to the anode cylinder is expected to yield a more robust water-cooled anode capable of much higher currents.

Electrical Configuration

As depicted in Figure 4.4, the experiment was set up in a triode configuration. The heater was connected to an Amrel 32 V, 400 A power supply. The keeper plate was powered by a Sorensen 150 V, 20 A supply. A 50 Ω resistor was placed between the keeper and the Sorensen supply to make it a less attractive pathway for current compared to the anode circuit. The anode was connected to this Sorensen supply and to a Rapid DC 35 V, 650 A supply through diodes; the cathode was grounded.

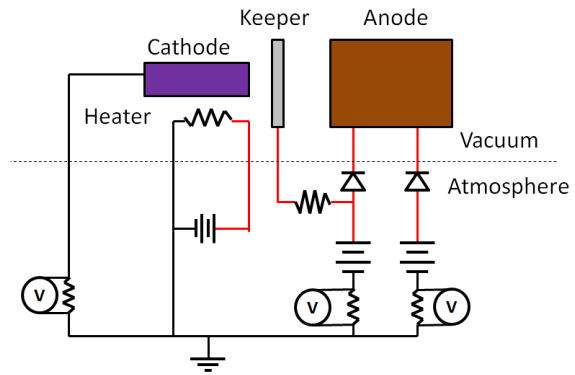


Figure 4.4: An electrical diagram for the RFC Cathode experiment.

This diode-based electrical circuit allows the keeper power supply's voltage (150 V) to bias both the anode and keeper plate until the lower voltage (35 V) primary anode supply can draw sufficient current to further lower the discharge voltage. At this point the configuration of the diodes causes the keeper to become electrically isolated from the anode. This allows the keeper and anode to be run simultaneously, in parallel, even if their respective power supplies are providing disparate voltages (allowing the anode to bias to the higher of the two supply voltages).

Neutral Gas Input

Argon or krypton gas was injected internally through the cathode as seen in Figure 4.1 and described previously in Section 4.1.1. The input mass flow rate was monitored using a variable-area flow meter (also known as a rotometer) capable of processing 0-120 SCCM (0.0-3.6 mg/s) of argon or 0-80 SCCM (0.0-5.0 mg/s) of krypton.

4.3 Diagnostics

Data have been collected to assess the performance of the RFC Cathode including current-voltage traces and axial temperature profiles along the length of the emitter region. The dependence of these data on neutral gas type as well as the adjustable parameters of mass flow rate and anode discharge current forms the basis of our initial characterization. For the temperature measurements, the higher heater powers required due to incomplete heat shielding was accepted in exchange for thermocouple access to the emitter region.

We assume that a profile of the temperature along the length of the emitter region can serve as a proxy for current density along the length. Therefore, variation in the current density inside the cathode is shown as variation of the temperature profile on the cathode surface. Measurement of the cathode temperature profile at different

operating points (varying the parameters listed above) allows for a relative comparison of profiles and a qualitative understanding of the trends. As noted by Polk, et al. [73], we do not expect our measurements of the outside surface of the cathode to match or have a constant offset from the temperature of the inside surface of the emitter. However, a temperature profile, even of the outside surface, is a relatively straightforward method that could provide evidence of the extent and uniformity of the plasma attachment when compared relative to different operating conditions.

The temperature profile along the length of the emitter region was measured at the outer surface of the graphite tube at four different locations (7.9 cm, 5.4 cm, 3.2 cm and 0.64 cm from the inner surface of the orifice plate) using 36-gauge, tungsten-rhenium C-type thermocouples. These thermocouples were insulated by the manufacturer in hafnia which was then coated with molybdenum to an outer diameter of 0.16 cm. These thermocouples were further insulated by a high-temperature zirconia paste and high temperature ceramic tubes (Omega PTR-A). This secondary layer of zirconia and ceramic tube was applied as a precaution due to operating in a carbon environment and due to damage observed in one instance, possibly from direct contact with the tungsten heater wire during operation. The temperature of the input and output water of the anode cooling lines was also monitored using two K-type thermocouples to provide another measure of the power flowing to the anode. T-type thermocouples were placed on two vacuum tank windows as the heater can partially radiate to the tank interior, warranting thermal monitoring of these components. All thermocouple readings were independently transmitted wirelessly (via Omega UWTC-1's) to a receiver outside the tank to be recorded by a computer.

Additionally, we measured the temperatures of the tungsten wire heater near the center of the LaB₆ emitter length, the tungsten orifice plate, and the boron nitride microwave window using a disappearing-filament optical pyrometer (Leeds & Northrup Model 8622-C) [74]. We calibrated the pyrometer against a cavity blackbody source

(Infrared Systems Development Corporation) to establish a maximum calibration error of 4% from the reference temperature. The pyrometer measures radiance at a single wavelength of 650 nm. We made emissivity corrections using the emissivity values at this wavelength for tungsten (0.44 with an estimated error of ± 0.05) and boron nitride (0.31 ± 0.10) [75–77]. The transmissivity of poly(methyl methacrylate), or acrylic, at 650 nm [78, 79] was also incorporated into the final emissivity correction since the measurements had to be made through acrylic vacuum tank windows. The estimated error of the emissivity values was added to the known error of the pyrometer measurement for the results reported.

Three shunt resistors with an error of 0.01% of the full scale were used to measure the cathode, anode, and keeper currents. Anode, keeper, and heater voltages were measured using voltage dividers connected between those components and ground. Sampling was done at 4 kHz, averaging 2000 samples per data point, with one set of samples being taken each second. These diagnostics were read using a National Instruments DAQ and monitored with LabView software on a computer.

4.4 Operational Ignition Procedure

After installation in the facility, the system was evacuated to the base pressure of 6×10^{-5} Torr and the heating cycle started. The heater current was gradually increased to 120-130 A over twenty minutes, delivering up to 4 kW of power at maximum current and voltage (132 A, 31.8 V). The neutral gas flow was initiated and set to various values depending on gas species. The cathode supply was set to 35 V while the keeper supply was turned on but limited to zero current. Once the maximum thermocouple temperature reached around 1400 °C, the heater supply was shut off and the keeper voltage was turned up. This cold start procedure [80] prevented arcing and current attachment to the heater. The keeper plasma stabilized with keeper volt-

ages ranging roughly between 25-40 V (at 20 A). Once the discharge had stabilized, the heater was turned on again to aid the transition into high-current operation. This transition took a few minutes to occur, after which the discharge current was turned up to at least 100 A to secure a stable plasma. The heater was then turned off as the fully established discharge became self-sustaining at voltages below the anode supply limit. The anode current limit could then be set at the desired operating condition until steady-state operation was reached. Fig. 4.5 shows the RFC Cathode experiment operating without RF at two different discharge currents.



Figure 4.5: The RFC Cathode operating at high discharge current on the left and at a lower current on the right. The downstream anode exit is at the left in the photos and the cathode is on the right. Although not distinguishable, the cathode plume is forming a few-centimeter diameter beam just beyond the keeper plate, signaling “jet” mode operation.

4.5 Experimental Results and Discussion

4.5.1 Ignition and Non-RF Operation

Following the operational procedure described in Section 4.4, the steady-state pre-ignition temperature profile shown in Fig. 4.7 was obtained repeatedly (± 30 C, 95% confidence). The locations of the temperature measurements are given in Fig. 4.6. Figure 4.8 shows the voltages required to start the cathode discharge (applied using the keeper supply) for a range of argon and krypton flow rates. It is relevant for future

large-cathode design and operation to note that much higher argon flow rates were required to achieve similar ignition voltages than those obtained using krypton (up to 80 SCCM more for argon at the same ignition voltage, or up to a 40 V difference for comparable flow rates).

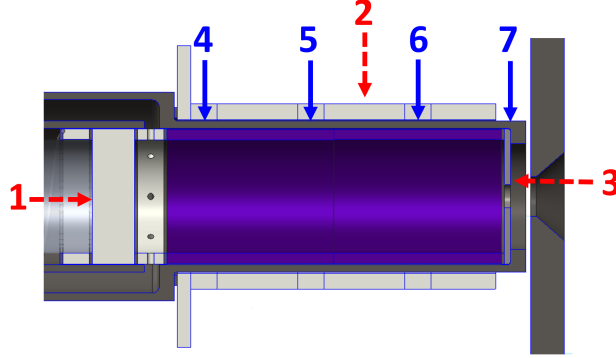


Figure 4.6: Locations of temperature measurements. 1-3 in red are pyrometer measurement locations (1 is the window, 2 is the heater wire, and 3 is the orifice plate) and 4-7 in blue are thermocouple measurements of the outer graphite surface of the cathode emitter region. (Slots exist in the boron nitride insulators for the thermocouples to touch the cathode wall directly.)

For low-current operation at approximately 20 A of anode current, we found that the steady-state voltages (Fig. 4.9) and cathode temperatures (Fig. 4.10) tended to decrease with increasing flow rate, and shifted substantially with changes in the gas type. All of the measured thermocouple temperatures along the cathode body showed a decreasing trend with increasing flow rate, in contrast to the trend in orifice plate behavior reported in Ref. 33.

The RFC Cathode was able to reach stable operation at a range of argon and krypton flow rates at a current of approximately 20 A. This current is comparable to the minimum self-heating condition presented for Goebel’s 2 cm LaB₆ hollow cathode [31], although the discharge voltage is much higher likely due to differences in thermal insulation and gas species. We found that initiating a discharge between the cathode and keeper, and even extracting small currents to the anode (≈ 20 A)

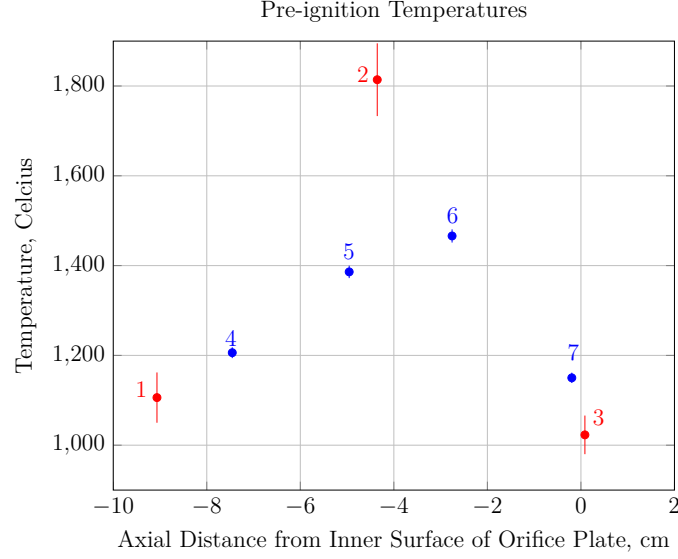


Figure 4.7: Temperature measurements taken prior to plasma ignition as a function of the distance from the inner surface of the orifice plate along the cathode major axis. 1-3 in red are pyrometer measurements (1 is the microwave window, 2 is the heater wire, and 3 is the orifice plate) and 4-7 in blue are thermocouple measurements of the outer cathode surface.

could be effected with relative ease; causing the anode to pull larger currents proved to be more difficult for the gases and power supplies used. In order to transition to high-current operation, the full keeper supply current (split predominantly toward the anode) was maintained and the heater was reactivated up to 4 kW in order to reduce the discharge voltage to below 35 V (the voltage limit for our high-current anode supply). For the tested configuration, we could only meet this power-supply-induced restriction using krypton. We have drawn anode currents up to 250 A with krypton, and expect to be able to draw much higher currents up to 400 A with our current infrastructure with an improved water-cooled anode.

Steady-state operation was achieved for anode currents between 20 and 225 A using krypton, though for currents below 30 A the discharge voltage surpassed the limit of our high-current supply. The voltage behavior of the RFC Cathode as a function of current for a fixed flow rate of $42 (\pm 2)$ SCCM krypton and a fixed keeper current of 2.2 A is shown in Fig. 4.11. The minimum or dip in the anode voltage and

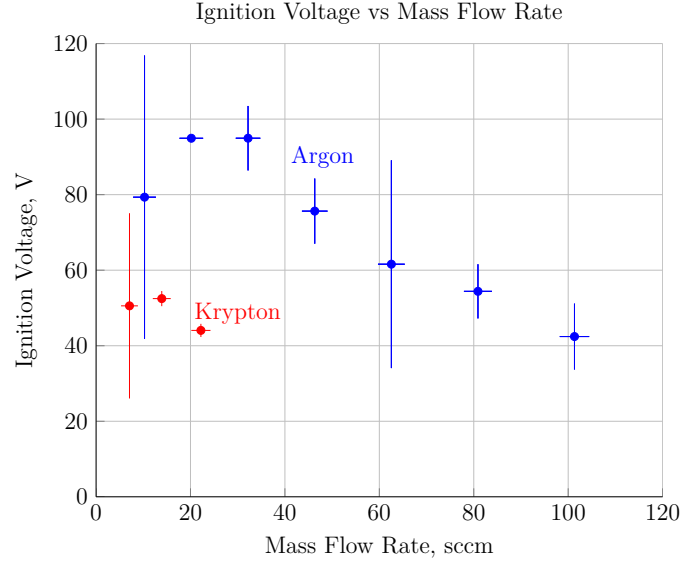


Figure 4.8: Discharge initiation voltage as a function of internal mass flow rate in SCCM for selected operating points using argon and krypton gas.

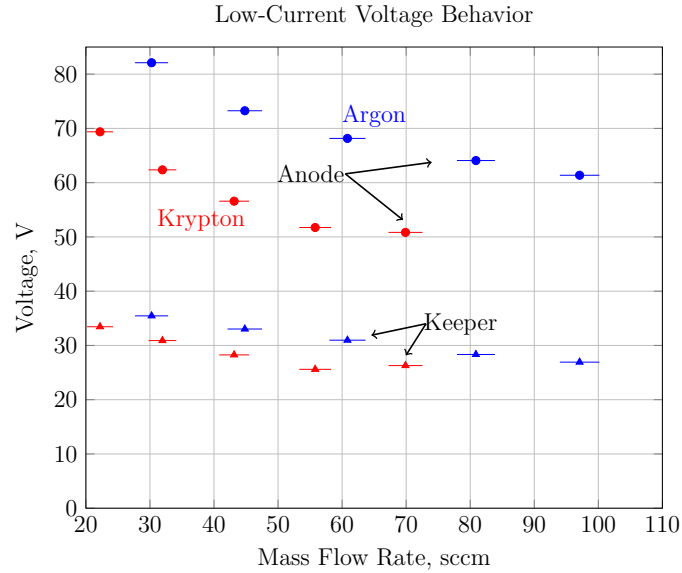


Figure 4.9: A comparison of the anode and keeper voltages versus mass flow rate for argon and krypton at approximately 20 A anode current.

the essentially monotonic decrease in keeper voltage as anode current is increased are expected qualitative behaviors and have been observed in the literature [22, 31].

The steady-state thermocouple temperatures as a function of discharge current at the previously mentioned operating condition with krypton are shown in Fig. 4.12.

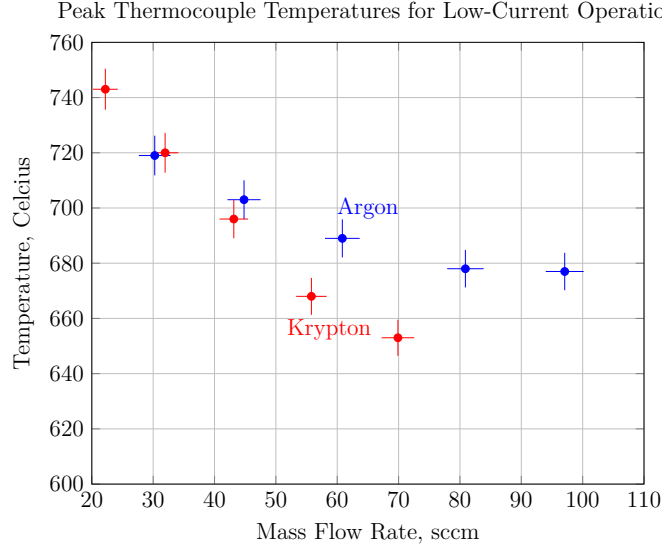


Figure 4.10: A comparison of peak thermocouple measurements versus mass flow rates of krypton and argon. The mass flow rates for each gas are offset from each other due to different flow meter corrections for each gas.

It is noteworthy that while the RFC Cathode operates at higher discharge voltages than those for prior cathodes [22, 31], it appears to operate at lower temperatures, especially near the orifice. Goebel’s 2 cm cathode operates at temperatures between 1500 and 2200 °C at the orifice plate [37], whereas the closest thermocouple to the cathode orifice plate in our configuration never exceeded 800 °C for the currents tested. It is important to note that this thermocouple measurement is not a direct measure of the orifice temperature, but still provides information regarding the maximum orifice temperature. Rather than at the closest location to the orifice, the maximum thermocouple temperature occurred at the next upstream measurement location (thermocouple #6 in Fig. 4.12).

The variation in temperature along the cathode tube length is much larger than the 5% variation in emitter temperature along the emitter length reported for prior large cathodes [31]. The variation in temperature along the cathode tube and the location of the maximum temperature are consistent across the tested discharge currents, though the thermocouple measurements of the cathode tube are not necessarily

representative of the emitter temperatures or their variation along the cathode length. These observations suggest that the current setup of the RFC Cathode operates at lower, but less-uniform, temperatures than comparably sized laboratory LaB_6 cathodes at the same currents. Possible reasons for a strongly peaked axial temperature variation include incomplete shielding, less thermally-isolated shielding overall, the boron nitride insulating rings along the emitter section causing non-uniform thermal conduction, and larger effective cross-sectional areas due to size at both the downstream end(orifice plate) for radiative losses and the upstream end for conductive losses (two large cathode tubes, even though wall thickness is minimized). More direct measurements will be needed to determine if these temperature variations are consistent between the cathode tube and emitter itself.

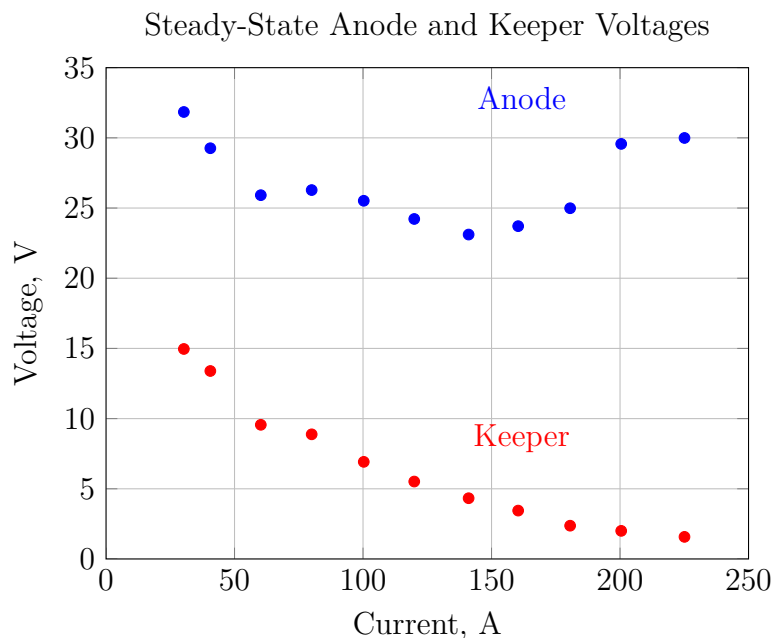


Figure 4.11: Anode and keeper voltages versus anode current for operation with krypton. The keeper current was held constant at 2.2 A and the mass flow rate was fixed at 42 SCCM. The measurement error bars are smaller than the plot markers used.

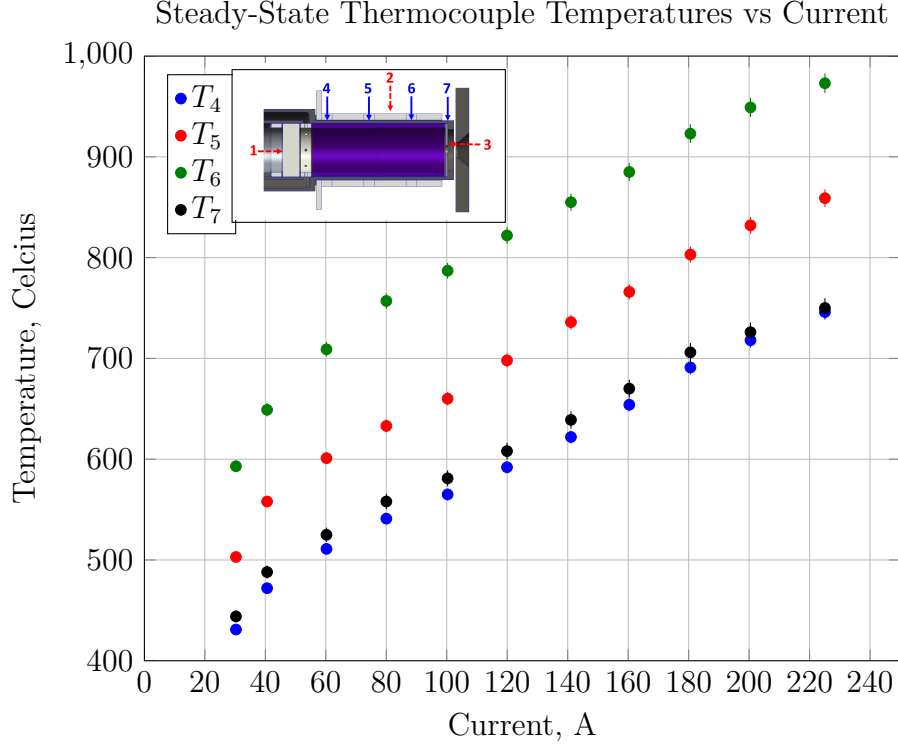


Figure 4.12: Thermocouple temperatures vs discharge current at a constant mass flow rate of 42 SCCM and 2.2 A keeper current.

4.5.2 Heater Failure Modes

We have experienced multiple heater failures during operation. Failures are often presaged by degradation in the heater as evidenced by an increase of the heater circuit resistance. While multiple factors seen in the literature like thermal gradients, nonuniform vaporization, and hot spots inherent to tungsten filaments can cause them to fail [81], these failures generally occur over longer timescales (hundreds of hours or more) than those observed during this experiment. At worst, we observed a heater failure in two brief, but high-temperature, thermal cycles. Since there are no significant mechanical loads on the wire, the likely short term causes of failure are arcing or material interactions. We expect that one of these causes is dominant for all of our failure cases.

Arcing failures of the heater can be correlated to witnessing events during experimentation, usually resulting in failure soon after. Post-run inspection of the wire reveals clear melting at the break joint. The prevalence of arcing failures was exacerbated by exploration of the operational envelope and the ignition procedure. However, since iterating the design and learning the appropriate parameters for igniting and operating the RFC Cathode, we have not had significant arcing problems. Arcing would be solved robustly if a suitable insulating ceramic and fabrication process were found that could completely isolate the heater wire and withstand temperatures approaching 2000 °C, or if a new heater was designed, potentially using a different material like graphite.

The second short-term cause of heater failure we have witnessed is material interaction. As seen in Fig. 4.13, visible damage is incurred by both the tungsten wire and boron nitride insulating rings during operation. This damage only occurs where the tungsten and boron nitride are in contact and furthermore, wire breaks of this nature only occur along these damaged areas of contact. To explain the source mechanism behind this failure, the literature explains that bulk tungsten and boron nitride can start to interact chemically to produce various tungsten borides when in contact and at temperatures starting between 800 and 1200 °C [82–85]. The quantity of the various tungsten borides created increases with both time and temperature. From Ref. 82 we calculated the expected cross-sectional area of boron diffusion to be greater than 7% of our original tungsten wire cross-section when operated at 1400 °C for 30 minutes. Pyrometer measurements of our bare tungsten heater wire in Fig. 4.7 show that the heater is often at much higher temperatures than this, and at the edge of our operational envelope, the heater temperature has peaked at over 1800 °C.

Tungsten borides are more resistive and have a different thermal expansion coefficient than tungsten [82,86–88] and are known to be brittle [82,83]. The mechanism by which we expect these heater failures occur starts with the formation of tungsten

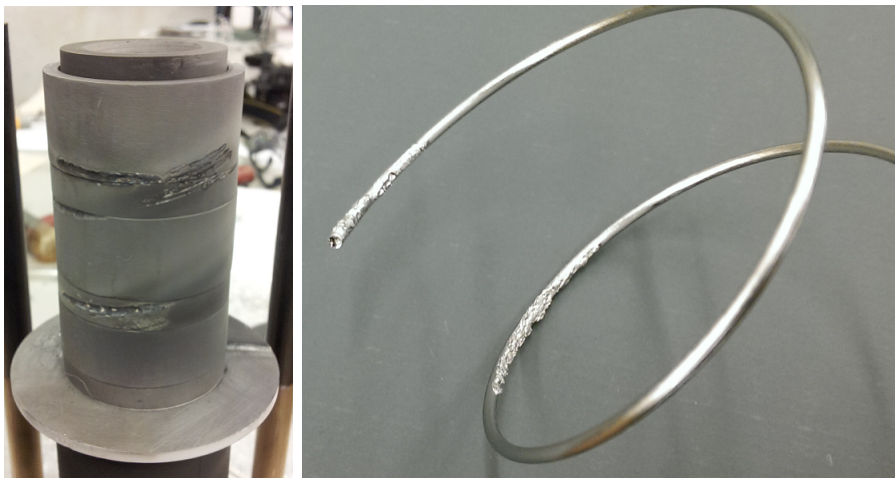


Figure 4.13: Pictured are examples of damaged boron nitride rings (left) and broken tungsten heater wire (right).

borides on the tungsten heater. The tungsten borides' higher resistivity than tungsten locally increases the temperature at a given heater current. This local heating aggravates cracking due to the difference in thermal expansion between the tungsten substrate and surface tungsten borides. The embrittled region experiences strong temperature gradients and increasing stress from differential thermal expansion until failure occurs. This is the suspected physical mechanism by which failure in this type of large-diameter cathode heater occurs.

As a possible solution to the material interaction problem, we have tested using graphite wire beads to separate the tungsten from the boron nitride. We assume most of the heat transfer is accomplished through radiation since the heater wire is typically in little direct contact with the insulating rings. Carbon beads do not seem to significantly change the thermal contact in our case. The carbon and tungsten could interact but carburization is usually slow and incomplete in a vacuum or argon environment. Tungsten carbide is not as brittle as tungsten borides and so we do not expect their potential creation at the surface to lead to a similar failure as demonstrated with tungsten borides [88].

Chapter 5

Conclusions

In exploring new concepts for high-current, long-life hollow cathodes, we have studied the novel concept of combining a thermionic hollow cathode and an RF cathode to find out if a microwave plasma can beneficially enhance the plasma structure of a thermionic cathode. The questions we posed initially are:

- Can we control the internal plasma structure of a thermionic hollow cathode by adding RF power in such a way so as to increase the cathode's operational lifetime and maximum discharge current?
- What are the challenges of scaling the inner diameter of a thermionic hollow cathode significantly larger?

We have pursued these questions through both numerical modeling and experimentation. Although the findings presented in this thesis are hardly the final answer to these questions, we have laid some of the foundation for future study and discovery.

5.1 Summary of Major Findings

5.1.1 Numerical Modeling Findings

From our modeling we found three major effects that result from the addition of RF power in the tens to few hundred watts:

1. With increasing RF power the plasma density increases significantly over most of the emitter length,
2. Increasing the RF power causes the axial location of densest plasma region to shift upstream on the order of millimeters to centimeters,
3. A nonlinear transition occurs in the plasma density, upstream electron temperature, emitted current, and RF power absorption which is dependent on the neutral gas pressure, the phase of the incident electric field, and the incident RF power.

The first two of these RF effects are improvements towards reaching our goal of a broader axial profile of the plasma density. Although the results do not necessarily indicate a flatter profile, they do suggest that added RF power increases insert utilization over significant axial distances, i.e., centimeters. This corresponds to creating a similar plasma upstream of the typical emitter-region cathode plasma to promote a broader plasma density profile that ensures a significant current-carrying plasma density along entire the emitter length.

The third finding of the nonlinear transition observed in our model also is beneficial to our goals, as it is a mechanism that can produce plasma densities an order of magnitude higher over most of the emitter with relatively little RF power input. In addition, we observed a hysteresis effect where high plasma densities are maintained post-transition although the RF power is lowered to pre-transition levels. The

transition and hysteresis behaviors are not uncommon as they are found in both experimental and numerical studies of microwave plasmas [34, 67–71]. This cathode concept is particularly promising if these behaviors are experimentally verified as modeled.

Without RF added, we found in our modeling that a large cathode inner-diameter does benefit the plasma density axial profile by broadening over a significant distance, in our case a majority of the 9 cm internal cathode length modeled. The limitation here is that we do not take into account orifice and external plasma effects to the internal profile.

5.1.2 Experimental Findings

Although we do not present experimental data on the addition of RF power to a large-diameter cathode in this thesis, we have taken significant steps in characterizing the initial operation of the largest LaB₆ thermionic hollow cathode to date. From the RFC Cathode experiment we not only want to build towards experimental verification of our modeled findings with added RF, but in this thesis we illuminate the design and operational challenges of large-diameter hollow cathodes. For the latter, we found that the thermal shielding, the cathode thermal design, and the heater design all strongly affect the performance and operational parameters of a thermionic cathode. These expected factors are particularly prominent when working with a large-diameter cathode as is shown by our 4 kW heater input power versus 0.4 kW for the next largest cathode [30].

These high heater powers have led to peak heater temperatures of over 1800 °C. To handle this high-temperature regime, current state-of-the-art solutions are not feasible. The high heater powers and high-temperature regime required new heater designs, specific refractory materials, and appropriately safeguarding the diagnostics, such as electrically-isolating each thermocouple independently with a correspond-

ing wireless relay device.¹ In iterating on a new heater design we found that bare, high-temperature tungsten-wire heaters can often fail due to arcing and undesirable material interactions. This example illustrates the key challenge of thermal design for large-diameter thermionic cathodes.

We have found that the RFC Cathode operates in a self-heating mode at a similar minimum current to other large cathodes (≈ 20 A), despite a large difference in scale [31]. However, we had difficulty transitioning to the full operating current range due to the relatively high voltages required for the large cathode with our available power supplies and neutral gases (argon and krypton). While a direct comparison of discharge voltages for given output currents between the RFC Cathode and other laboratory cathodes provides limited insight due to thermal design and gas species differences, the voltage behavior of the cathode follows previously observed non-monotonic trends with increasing discharge current [30–32, 42].

The thermal behavior of the RFC Cathode, however, strays significantly from the measurements reported in the literature. First, we made what is effectively a proxy for an orifice plate temperature measurement by using a thermocouple in contact with the cathode tube directly adjacent to the orifice plate (#7 in Fig. 4.6). To support the similarity of this proxy to the actual measurement, Fig. 4.7 shows an actual pyrometer measurement of the orifice plate (#3 in Fig. 4.7) which is lower in temperature than the proxy thermocouple temperature (#7). Both measurements are within approximately 100 °C of each other. Comparing this proxy orifice plate temperature measurement across discharge currents shown in Fig. 4.12 with the literature [30, 31, 33], we find that the RFC Cathode operates at dramatically lower temperatures across discharge currents. In fact, even assuming a large error of a few hundred degrees within our proxy orifice plate measurement, our large-diameter cathode is operating at temperatures of 100’s to roughly 1000 °C *less* than other

¹At least one cathode thermocouple had a critical insulator failure, which in turn rendered the corresponding wireless relay device electrically damaged and unusable.

large cathodes! Although starting the cathode may require high heater powers and corresponding high-temperatures due to thermal design and size, once operating, the large-diameter cathode appears to operate at much lower temperatures than previous thermionic cathodes.

Secondly, at low discharge currents the RFC Cathode displays a temperature trend with increasing mass flow rate that opposes previously reported trends in orifice temperature [33]. Finally, we found that the variation of the axial temperature profile varies widely and observe a peak which is distanced from the orifice. We found the measured temperature profile peak is uniquely distanced from the orifice when compared the literature [2,32,43], which we expect to be driven by the cathode orifice size, the inner diameter of the cathode, and the thermal design of the RFC Cathode.

In summary, we have setup and tested a large-diameter cathode experiment, made initial progress in characterizing the cathode, and have identified the significant challenges to designing and operating such a cathode. By iterating on solutions to these identified challenges, data can be collected with the RF power added to compare experimental RFC Cathode findings with the numerically-modeled findings presented.

5.2 Recommendations for Future Work

Planned future work includes further characterization of the large-diameter RFC Cathode without added RF power, necessary experimental improvements, and the determination of the effects of adding RF power. Further characterization efforts can be aimed at investigating the much lower operating temperatures observed, exploring the level of correspondence between the cathode axial temperature profile to the emitter profile, and operating the cathode with xenon to get a closer voltage comparison to other cathodes across discharge currents. As the large-diameter of the RFC

Cathode is pushing the envelope of thermionic hollow cathode size, the experimental and design challenges identified must be addressed first.

A major experimental challenge is improving the thermal design of the RFC Cathode which includes thermal shielding and heater design. With a better shielding strategy the required heater power will be minimized. Better shielding may also help improve the currently wide variation in the axial cathode temperature profile. In order to obtain significant testing hours without heroics, the heater failure problem must be addressed with a more robust design. This could include different insulator or heater materials. As our research on high-temperature heaters is exploratory, we expect that there is significant progress yet to be made in this area for large-scale thermionic hollow cathodes.

Another experimental challenge is the relatively high voltage required to operate the large-diameter cathode in our initial testing, although starting ignition voltages have all been relatively low, under 100 V. Clearly, the gas species significantly affects both the plasma ignition voltage and operating voltage for a given discharge current. This operating voltage behavior for a large-diameter cathode quickly becomes a cost trade-off: Access to costly power supplies that are capable of both high currents and voltages, or investment in xenon gas (or secondarily, krypton) with the lowest expected voltage requirements. Further reductions in operating voltage are likely possible by addressing other system effects, though gas species is likely predominant.

Finally, three further areas of experimental improvement to be made regarding the addition of RF power are: improving the robustness of the microwave window/gas break at the vacuum tank wall, adding a diagnostic to measure if any gas leaks (or any plasma is created) in the upstream waveguide, and adding the ability to more stably tune the cathode microwave cavity. Although data collection with added RF power was attempted, the vacuum tank gas break failed on early attempts and tuning the microwaves to the varying-impedance plasma proved to be challenging as expected.

However, the aforementioned improvements should allow for successful data collection while adding RF power.

With promising numerical-modeling results and an operating large-diameter cathode experiment, the RF-Controlled Cathode warrants further experimentation with added RF power in order to judge this novel concept on the basis of high-current, long-lifetime operation.

Bibliography

- [1] Robert G Jahn and Edgar Y Choueiri. *Electric Propulsion*, 2002.
- [2] Dan M Goebel and Ira Katz. *Fundamentals of Electric Propulsion: Ion and Hall Thrusters*. John Wiley & Sons Inc, 2008.
- [3] W Andrew Hoskins, R Joseph Cassady, Olwen Morgan, Roger M Myers, Fred Wilson, David Q King, and Kristi DeGrys. 30 Years of Electric Propulsion Flight Experience at Aerojet Rocketdyne. In *33rd International Electric Propulsion Conference*, 2013.
- [4] Rainer Killinger, Ralf Kukies, Michael Surauer, Angeo Tomasetto, and Leo van Holtz. ARTEMIS orbit raising inflight experience with ion propulsion. *Acta Astronautica*, 53(4-10):607–621, 2003.
- [5] Steven A. Feuerborn, Julie Perkins, and David A. Neary. Finding a Way: Boeing’s All Electric Propulsion Satellite. In *49th AIAA/ASME/SAE/ASEE Joint Propulsion Conference*, 2013.
- [6] John R. Brophy. NASA’s Deep Space 1 ion engine (plenary). *Review of Scientific Instruments*, 73(2):1071, 2002.
- [7] Christophe R Koppel and Denis Estublier. The Smart-1 Electric Propulsion Subsystem. In *39th AIAA/ASME/SAE/ASEE Joint Propulsion Conference*, 2003.
- [8] Hitoshi Kuminaka, Kazutaka Nishiyama, Ikko Funaki, Tetsuya Yamada, Yukio Shimizu, and Jun’ichiro Kawaguchi. Powered Flight of Electron Cyclotron Resonance Ion Engines on Hayabusa Explorer. *Journal of Propulsion and Power*, 23(3):544–551, 2007.
- [9] John R Brophy, Michael G Marcucci, Gani B Ganapathi, Charles E Garner, Michael D Henry, Barry Nakazono, and Don Noon. The Ion Propulsion System for Dawn. In *39th AIAA/ASME/SAE/ASEE Joint Propulsion Conference*, 2003.
- [10] Charles E Garner and Marc D Rayman. In-Flight Operation of the Dawn Ion Propulsion System Through Survey Science Orbit at Ceres. In *51st AIAA/ASME/SAE/ASEE Joint Propulsion Conference*, 2015.
- [11] John R. Brophy, Louis Friedman, and Fred Culick. Asteroid Retrieval Feasibility Study. In *IEEE Aerospace Conference Proceedings*, number April, 2012.

- [12] Matthew L Plasek, Christopher J Wordingham, Sebastian Rojas Mata, Nicolas Luzarraga, Edgar Y Choueiri, and James E Polk. Experimental Investigation of a Large-Diameter Cathode. In *50th AIAA/ASME/SAE/ASEE Joint Propulsion Conference*, 2014.
- [13] Rohit Shastry, Daniel A Herman, George C Soulas, and Michael J Patterson. NASA’s Evolutionary Xenon Thruster (NEXT) Long-Duration Test as of 736 kg of Propellant Throughput. In *48th AIAA/ASME/SAE/ASEE Joint Propulsion Conference*, 2012.
- [14] Rohit Shastry. Status of NASA’s Evolutionary Xenon Thruster (NEXT) Long-Duration Test as of 50,000 h and 900 kg Throughput. In *33rd International Electric Propulsion Conference*, Washington, D.C., 2013.
- [15] Richard R Hofer, Thomas M Randolph, David Y Oh, John Steven Snyder, and Kristi H de Grys. Evaluation of a 4.5 kW Commercial Hall Thruster System for NASA Science Missions. In *42nd AIAA/ASME/SAE/ASEE Joint Propulsion Conference*, 2006.
- [16] Steven R Oleson. Electric Propulsion Technology Development for the Jupiter Icy Moons Orbiter Project. In *40th AIAA/ASME/SAE/ASEE Joint Propulsion Conference*, 2004.
- [17] John R. Brophy and Muriel Noca. Electric Propulsion for Solar System Exploration. *Journal of Propulsion and Power*, 14(5):700–707, 1998.
- [18] Roland Edward Florenz. *The X3 100-kW Class Nested-Channel Hall Thruster: Motivation, Implementation and Initial Performance*. PhD thesis, University of Michigan, 2014.
- [19] Daniel L Brown, Brian E Beal, and James M Haas. Air Force Research Laboratory High Power Electric Propulsion Technology Development. In *IEEEAC*, 2009.
- [20] Dan M. Goebel, Kristina K. Jameson, and Richard R. Hofer. Hall Thruster Cathode Flow Impact on Coupling Voltage and Cathode Life. *Journal of Propulsion and Power*, 28(2):355–363, 2012.
- [21] James E. Polk, Hani Kamhawi, Kurt Polzin, John Brophy, John Ziemer, Timothy D Smith, and Mike Lapointe. An Overview of NASA’s Electric Propulsion Programs, 2010-11. In *32nd International Electric Propulsion Conference*, 2011.
- [22] Dan M. Goebel and Emily Chu. High Current Lanthanum Hexaboride Hollow Cathodes for High Power Hall Thrusters. In *32nd International Electric Propulsion Conference*. Jet Propulsion Laboratory, 2011.
- [23] George C Soulas, Thomas W Haag, Daniel A Herman, Wensheng Huang, Hani Kamhawi, and Rohit Shastry. Performance Test Results of the NASA-457M v2

- Hall Thruster. In *48th AIAA/ASME/SAE/ASEE Joint Propulsion Conference*, 2012.
- [24] Scott J. Hall, Roland E. Florenz, Alec Gallimore, Hani Kamhawi, Daniel L. Brown, James E. Polk, Dan M. Goebel, and Richard R. Hofer. Implementation and Initial Validation of a 100-kW Class Nested-channel Hall Thruster. In *50th AIAA/ASME/SAE/ASEE Joint Propulsion Conference*, 2014.
 - [25] J Slough, D Kirtley, and Thomas Weber. Pulsed plasmoid propulsion: The ELF Thruster. In *31st International Electric Propulsion Conference*, 2009.
 - [26] A. D. Kodys and Edgar Y. Choueiri. A Critical Review of the State-of-the-Art in the Performance of Applied-field Magnetoplasmdynamic Thrusters. In *41st AIAA/ASME/SAE/ASEE Joint Propulsion Conference*, 2005.
 - [27] Edgar A Bering, Matthew Giambusso, Mark Carter, Andrew Ilin, Chris S Olsen, Jared P Squire, Franklin R Chang Díaz, and Benjamin W Longmier. Using VASIMR for the Proposed Europa Mission. In *AIAA Space 2014 Conference*, 2014.
 - [28] Hani Kamhawi, David H Manzella, Timothy D Smith, and George R Schmidt. High-Power Hall Propulsion Development at NASA Glenn Research Center. In *63rd International Astronautical Congress*, 2014.
 - [29] Ioannis G. Mikellides, Dan M. Goebel, Benjamin A Jorns, James E Polk, and Pablo Guerrero. Numerical Simulations of the Partially-ionized Gas in a 100-A LaB 6 Hollow Cathode. *IEEE Transactions on Plasma Science*, 43(1):1–15, 2015.
 - [30] Dan M. Goebel and Emily Chu. High Current Lanthanum Hexaboride Hollow Cathode for 20-to-100 kW Class Hall Thrusters. In *48th AIAA/ASME/SAE/ASEE Joint Propulsion Conference*, 2012.
 - [31] Dan M. Goebel and Emily Chu. High-Current Lanthanum Hexaboride Hollow Cathode for High-Power Hall Thrusters. *Journal of Propulsion and Power*, 30(1):35–40, 2014.
 - [32] Jonathan L. Van Noord, Hani Kamhawi, and Heather K. McEwen. Characterization of a High Current, Long Life Hollow Cathode. In *29th International Electric Propulsion Conference*, 2005.
 - [33] Hani Kamhawi and Jonathan Van Noord. Development and Testing of High Current Hollow Cathodes for High Power Hall Thrusters. In *48th AIAA/ASME/SAE/ASEE Joint Propulsion Conference*, 2012.
 - [34] Kevin D. Diamant. Resonant Cavity Plasma Electron Source. *IEEE Transactions on Plasma Science*, 37(8):1558–1562, 2009.

- [35] John E Foster and Michael J Patterson. Characterization of 40-Centimeter Microwave Electron Cyclotron Resonance Ion Source and Neutralizer. *Journal of Propulsion and Power*, 21(5):1–5, 2005.
- [36] Matthew L Plasek, Benjamin Jorns, Edgar Y Choueiri, and James E Polk. Exploration of RF-Controlled High Current Density Hollow Cathode Concepts. In *48th AIAA/ASME/SAE/ASEE Joint Propulsion Conference*. American Institute of Aeronautics and Astronautics, 2012.
- [37] Dan M. Goebel, Ron M. Watkins, and Kristina K. Jameson. LaB6 Hollow Cathodes for Ion and Hall Thrusters. *Journal of Propulsion and Power*, 23(3):552–558, 2007.
- [38] W. Schottky. Concerning the Discharge of Electrons from Hot Wires with Delayed Potential. *Annalen der Physik*, 44(15):1011–1032, 1914.
- [39] Ira Katz, Ioannis G Mikellides, Dan M Goebel, and James E Polk. Insert Heating and Ignition in Inert-Gas Hollow Cathodes. *IEEE Transactions on Plasma Science*, 36(5):2199–2206, 2008.
- [40] James E. Polk, Ioannis G. Mikellides, Ira Katz, and Angela M. Capece. Tungsten and Barium Transport in the Internal Plasma of Hollow Cathodes. *Journal of Applied Physics*, 105(11):113301, 2009.
- [41] Matthew L Plasek, Christopher J Wordingham, Edgar Y Choueiri, and James E Polk. Modeling and Development of the RF-Controlled Hollow Cathode Concept. In *49th AIAA/ASME/SAE/ASEE Joint Propulsion Conference*, 2013.
- [42] Dan M Goebel and Ronald M Watkins. Compact Lanthanum Hexaboride Hollow Cathode. *Review of Scientific Instruments*, 81(8):083504, 2010.
- [43] James E Polk, Angela M Capece, Ioannis G Mikellides, and Ira Katz. Barium Depletion in the NSTAR Discharge Cathode After 30,472 Hours of Operation. In *46th AIAA/ASME/SAE/ASEE Joint Propulsion Conference*, 2010.
- [44] Kristina K. Jameson, Dan M. Goebel, Richard R. Hofer, and Ron M. Watkins. Cathode Coupling in Hall Thrusters. In *30th International Electric Propulsion Conference*, 2007.
- [45] R.R. Hofer, L.K. Johnson, D.M. Goebel, and R.E. Wirz. Effects of Internally-Mounted Cathodes on Hall Thruster Plume Properties. *IEEE Transactions on Plasma Science*, 36(5):2004–2014, 2008.
- [46] Dan M. Goebel, Kristina K. Jameson, Ira Katz, and Ioannis G. Mikellides. Potential fluctuations and energetic ion production in hollow cathode discharges. *Physics of Plasmas*, 14(10):103508, 2007.

- [47] Dan M. Goebel, Kristina K. Jameson, Ira Katz, and Ioannis G. Mikellides. Plasma Potential Behavior and Plume Mode Transitions in Hollow Cathode Discharges. In *30th International Electric Propulsion Conference*, 2007.
- [48] Ioannis G. Mikellides, Ira Katz, Dan M. Goebel, Kristina K. Jameson, and James E. Polk. Wear Mechanisms in Electron Sources for Ion Propulsion, 2: Discharge Hollow Cathode. *Journal of Propulsion and Power*, 24(4):866–879, 2008.
- [49] Dan M Goebel, Ioannis G Mikellides, James E Polk, Jack Young, William G Tighe, and Kuei-ru Chien. Keeper Wear Mechanisms in the XIPS 25-cm Neutralizer Cathode Assembly. In *31st International Electric Propulsion Conference*, 2009.
- [50] Ioannis G. Mikellides, Dan M. Goebel, John Steven Snyder, Ira Katz, and Daniel a. Herman. The discharge plasma in ion engine neutralizers: Numerical simulations and comparisons with laboratory data. *Journal of Applied Physics*, 108(11):113308, 2010.
- [51] Benjamin A Jorns, Ioannis G Mikellides, and Dan M Goebel. Ion acoustic turbulence in a 100-A LaB6 hollow cathode. *Physical Review E*, 90(6):1–10, 2014.
- [52] Emily Chu, Dan M. Goebel, and Richard E. Wirz. Reduction of Energetic Ion Production in Hollow Cathodes by External Gas Injection. *Journal of Propulsion and Power*, 29(5):1155–1163, 2013.
- [53] Dan M Goebel, James E Polk, Izabela Sandler, Ioannis G Mikellides, J R Brophy, William G Tighe, and Kuei-ru Chien. Evaluation of 25-cm XIPS Thruster Life for Deep Space Mission Applications. In *31st International Electric Propulsion Conference*, 2009.
- [54] Ronald L Corey and David J Pidgeon. Electric Propulsion at Space Systems/Loral. In *31st International Electric Propulsion Conference*, Ann Arbor, Michigan, 2009.
- [55] Michael A Lieberman and Allan J Lichtenberg. *Principles of plasma discharges and materials processing*. John Wiley and Sons, 1994.
- [56] S K Jain, Akhilesh Jain, and P R Hannurkar. Indigenous development of a low cost high power 2 kW (CW), 2.45 GHz microwave system. *Indian Journal of Pure & Applied Physics*, 42:896–901, 2004.
- [57] D Windes, J Dutkowski, R Kaiser, and R Justice. Triservice-NASA cathode life test facility. *Applied Surface Science*, 146:75–78, 1999.
- [58] D Dieumegard, J C Tonnerre, D Brion, and A M Shroff. Life Test Performance of Thermionic Cathodes. *Applied Surface Science*, 111:84–89, 1997.

- [59] Samuel Y. Liao. *Microwave Devices and Circuits*. Prentice Hall, 3rd edition, 1990.
- [60] A Salhi and P J Turchi. Scaling Relations for Design and Operation of Orificed-Hollow Cathodes. In *30th AIAA/ASME/SAE/ASEE Joint Propulsion Conference*, 1994.
- [61] Matthew L Plasek, Christopher J Wordingham, and Edgar Y Choueiri. Resonant Mode Transition in the RF-Controlled Hollow Cathode. In *33rd International Electric Propulsion Conference*, 2013.
- [62] Ioannis G. Mikellides, Ira Katz, Dan M. Goebel, and James E. Polk. Hollow cathode theory and experiment. II. A two-dimensional theoretical model of the emitter region. *Journal of Applied Physics*, 98(11):113303, 2005.
- [63] B. A. Younglove and H. J. M. Hanley. Viscosity and Thermal Conductivity Coefficients of Gaseous and Liquid Argon. *Journal of Physical Chemistry*, 15(4), 1986.
- [64] J. M. Lafferty. Boride Cathodes. *Journal of Applied Physics*, 22(3):299, 1951.
- [65] T. J. Jones. *Thermionic Emission*. Methuen & Co, 1936.
- [66] G D Hobbs and J A Wesson. Heat flow through a Langmuir sheath in the presence of electron emission. *Plasma Physics*, 9:85–87, 1967.
- [67] Yu Zhu. *Modeling of a Microwave Plasma Electron Source for Neutralization of Ion Thrusters*. PhD thesis, University of Toulouse, 2013.
- [68] H Sugai, I Ghanashev, and M Nagatsu. High-Density Flat Plasma Production Based on Surface Waves. *Plasma Sources Science and Technology*, 7(2):192–205, 1998.
- [69] H. Sugai, I. Ghanashev, and K. Mizuno. Transition of electron heating mode in a planar microwave discharge at low pressures. *Applied Physics Letters*, 77(22):3523, 2000.
- [70] Ivan P Ganachev and Hideo Sugai. Production and control of planar microwave plasmas for materials processing. *Plasma Sources Science and Technology*, 11:A178–A190, 2002.
- [71] G. J. M. Hagelaar, K. Hassouni, and A. Gicquel. Interaction between the electromagnetic fields and the plasma in a microwave plasma reactor. *Journal of Applied Physics*, 96:1819, 2004.
- [72] WG Tighe, Ken Freick, and KR Chien. Performance evaluation and life test of the XIPS hollow cathode heater. In *41st AIAA/ASME/SAE/ASEE Joint Propulsion Conference*, 2005.

- [73] J E Polk, C M Marrese-Reading, B Thornber, L Dang, L K Johnson, and I Katz. Scanning optical pyrometer for measuring temperatures in hollow cathodes. *The Review of scientific instruments*, 78(9):093101, sep 2007.
- [74] Ketil Motzfeldt. *High Temperature Experiments in Chemistry and Materials Science*. John Wiley and Sons, 2012.
- [75] B. Muller and U. Renz. Development of a fast fiber-optic two-color pyrometer for the temperature measurement of surfaces with varying emissivities. *Review of Scientific Instruments*, 72(8):3366, 2001.
- [76] D Svet. *Thermal radiation: metals, semiconductors, ceramics, partly transparent bodies, and films*. Springer US, New York, 1st edition, 1965.
- [77] Aleksander Sala. *Radiant Properties of Materials: Tables of Radiant Values for Black Body and Real Materials*. Elsevier Science Ltd, 1986.
- [78] Jan W Gooch. *Encyclopedic Dictionary of Polymers*. Springer New York, 2nd edition, 2011.
- [79] C Joram. Transmission curves of plexiglass (PMMA) and optical grease. Technical Report October, CERN, PH-EP, 2009.
- [80] Jason A Vaughn, Todd A Schneider, and Miria M Finckenor. Life Testing of the Hollow Cathode Plasma Contactor for the ProSEDS Mission. In *7th Spacecraft Charging Technology Conference*, 2001.
- [81] O Horacek. Properties and failure modes of incandescent tungsten filaments. *IEEE Proceedings A*, 127(3), 1980.
- [82] M. Usta, I. Ozbek, M. Ipek, C. Bindal, and A.H. Ucisik. The characterization of borided pure tungsten. *Surface and Coatings Technology*, 194(2-3):330–334, 2005.
- [83] K A Khor, L G Yu, and G Sundararajan. Formation of hard tungsten boride layer by spark plasma sintering boriding. *Thin Solid Films*, 478:232–237, 2005.
- [84] Peter Rogl. Materials science of ternary metal boron nitrides. *International Journal of Inorganic Materials*, 3:201–209, 2001.
- [85] H Itoh, T Matsudaira, and S Naka. Formation process of tungsten borides by solid state reaction between tungsten and amorphous boron. *Journal of Materials Science*, 22:2811–2815, 1987.
- [86] CC Wang, SA Akbar, W Chen, and VD Patton. Electrical properties of high-temperature oxides, borides, carbides, and nitrides. *Journal of Materials Science*, 30:1627–1641, 1995.
- [87] HJ Juretschke and R Steinitz. Hall effect and electrical conductivity of transition-metal diborides. *Journal of Physics and Chemistry of Solids*, 4:118–127, 1958.

- [88] E Lassner and WD Schubert. *Tungsten*. Springer Science, 1999.